Absorption Filaments Towards the Massive Clump G0.253+0.016

John Bally [1], J. M. Rathborne [2], S, N. Longmore [3], J. M. Jackson [4], J. F. Alves [5], E. Bressert [6], Y. Contreras [7], J. B. Foster [8], G. Garay [9], A. Ginsburg [10], K. G. Johnston [11], J. M. D. Kruijssen [12], L. Testi [13], and A. J. Walsh [14]

[1] *Department of Astrophysical and Planetary Sciences,*
University of Colorado, UCB 389, Boulder, CO 80309

John.Bally@colorado.edu

[2] *CSIRO Astronomy and Space Science, P.O. Box 76, Epping NSW, 1710, Australia*

Jill.Rathborne@csiro.au

[3] *Liverpool Johns Moore University, Liverpool, England*

S.N.Longmore@ljmu.ac.uk

[4] *Institute for Astrophysical Research, Boston University, Boston, MA 02215, USA*

jackson@bu.edu

[5] *University of Vienna, Turkenschanzstrasse 17, 1180 Vienna, Austria*

joao.alves@univie.ac.at

[6] *CSIRO Astronomy and Space Science, P.O. Box 76, Epping NSW, 1710, Austraila*

ebressert@gmail.com

[7] *CSIRO Astronomy and Space Science, P.O. Box 76, Epping NSW, 1710, Austraila*

Yanett.Contreras@csiro.au

[8] *Yale Center for Astronomy and Astrophysics, Yale University, New Haven, CT 06520,*
USA

jonathan.b.foster@yale.edu

[9] *Universidad de Chile, Camino El Observatorio 515, Las Condes, Santiago, Chile*

guido@das.uchile.cl

arXiv:1409.3640v1 [astro-ph.GA] 12 Sep 2014

[10] *European Southern Observatory, Karl-Schwarzschild-Str. 2, 85748 Garching bei Munchen, Germany*

adam.g.ginsburg@gmail.com

[11] *Max Planck Institute for Astronomy, Heidelberg, Germany,*
School of Physics and Astronomy, University of Leeds, Leeds LS2 9JT, UK

johnston@mpia-hd.mpg.de

[12] *Max Planck Institut fur Astrophysik, Karl-Schwarzschild-Str. 2, Garching bei Munchen, Germany*

kruijssen@mpa-garching.mpg.de

[13] *European Southern Observatory, Karl-Schwarzschild-Str. 2, 85748 Garching bei Munchen, Germany*

ltesti@eso.org

[14] *International Centre for Radio Astronomy Research, Curtin University, GPO Box U1987, Perth, Australia*

andrew.walsh@curtin.edu.au

ABSTRACT

ALMA HCO^+ observations of the infrared dark cloud G0.253+0.016 located in the Central Molecular Zone of the Galaxy are presented. The 89 GHz emission is area-filling, optically thick, and sub-thermally excited. Two types of filaments are seen in absorption against the HCO^+ emission. *Broad-line absorption filaments* (BLAs) have widths of less than a few arcseconds ($0.07 - 0.14$ pc), lengths of 30 to 50 arcseconds ($1.2 - 1.8$ pc), and absorption profiles extending over a velocity range larger than 20 km s^{-1}. The BLAs are nearly parallel to the nearby G0.18 non-thermal filaments and may trace HCO^+ molecules gyrating about highly ordered magnetic fields located in front of G0.253+0.016 or edge-on sheets formed behind supersonic shocks propagating orthogonal to our line-of-sight in the foreground. *Narrow-line absorption filaments* (NLAs) have line-widths less than 20 km s^{-1}. Some NLAs are also seen in absorption in other species with high optical depth such as HCN and occasionally in emission where the background is faint. The NLAs, which also trace low-density, sub-thermally

excited HCO$^+$ molecules, are mostly seen on the blueshifted side of the emission from G0.253+0.016. If associated with the surface of G0.253+0.016, the kinematics of the NLAs indicate that the cloud surface is expanding. The decompression of entrained, milli-Gauss magnetic fields may be responsible for the re-expansion of the surface layers of G0.253+0.016 as it recedes from the Galactic center following a close encounter with Sgr A.

Subject headings: ISM: - molecular clouds – ISM: individual – G0.253+0.016 stars: formation – Central Molecular Zone

1. Introduction

The Central Molecular Zone (CMZ) at Galactocentric radii less than ∼500 pc contains the most massive, dense, and turbulent molecular clouds in the Galaxy (Rodriguez-Fernandez & Combes 2008; Ferrière et al. 2007; Rodriguez-Fernandez et al. 2006; Pierce-Price et al. 2000; Morris & Serabyn 1996; Bally et al. 1987b, 1988) along with some of the most compact and massive star clusters (Figer et al. 2002; Habibi et al. 2013).

Lis & Carlstrom (1994) found an exceptionally massive and dense cloud seen in projection against the bright near- and mid-infrared emission from the CMZ, G0.253+0.016. Located towards the brightest portion of the Galactic plane at infrared wavelengths, this cloud was clearly seen in silhouette against the CMZ in the IRAS mid-infrared images and is the most prominent infrared dark cloud (IRDC) in the sky (Menten et al. 2005; Arendt et al. 2008; Ramírez et al. 2008).

Lis et al. (1994) and Lis & Menten (1998) demonstrated that this cloud has an unusually high mass ($M > 10^5$ M$_\odot$) and density ($N(H_2) > 10^5$ cm^{-2}) and is very compact ($r < 3$ pc). Lis et al. (2001) used ISO data and millimeter-wave spectra to show that the dust temperature is low but the gas is hot. In the cloud center, $15 < T_{dust} < 22$ K but increases to ∼27 K at the cloud edges (Longmore et al. 2012). On the other hand, the gas is hot with $T_{gas} \sim 80$ K (Ao et al. 2013). The mid-infrared fine-structure cooling lines measured with ISO indicated that near-UV interstellar radiation field surrounding the cloud is about 10^3 times stronger than in the Solar vicinity (Lis et al. 2001), consistent with warmer dust at the cloud periphery. Kauffmann et al. (2013) presented interferometric SiO and N$_2$H$^+$ maps of G0.253+0.01 that exhibit some localized narrow spectral lines with central velocities covering the wide velocity range seen in single-dish data (Rathborne et al. 2014b). The large line-widths and bright emission in tracers such as SiO, and the complicated kinematics was interpreted as evidence for shocks, possibly indicating an early stage of a cloud-cloud collision

(Higuchi et al. 2014).

G0.253+0.016 (also known as the 'Lima Bean' or the 'Brick') has been proposed to be a possible progenitor to a massive star cluster (Longmore et al. 2012). Fitting the dust continuum SED to the Herschel 60, 160, 250, 350, and 500 μm data obtained from the Herschel Space Observatory Hi-GAL survey (Molinari et al. 2011, 2010a,b) and 1100 μm from the Bolocam Galactic Plane Survey (BGPS; Bally et al. 2010) reveals a dust temperature of ∼20 K, H_2 column density of ∼ 3.3×10^{23} cm^{-2}, and mass of ∼ 10^5 M$_\odot$ (Longmore et al. 2012, 2013). Absorption in the near- and far-infrared and application of the virial theorem to spectral line data (Rathborne et al. 2014b) give similar results for the mass and column density. With a mean radius of about 3 pc and a mean density $n(H_2) \approx 7 \times 10^4$ cm^{-3}, G0.253+0.016 has sufficient mass to potentially form a young massive cluster (Portegies-Zwart et al. 2010). However, previous studies found no evidence for internal heating sources or embedded HII regions (Lis et al. 2001). Only one H_2O maser has been found in G0.253+0.016 (Lis et al. 1994; Breen & Ellingsen 2011). Thus, G0.253+0.016 may either be in the very earliest stages of high-mass star or cluster formation, or because of the extreme conditions in the CMZ, may fail to form many stars.

Most star formation in the CMZ occurs on a twisted elliptical ring-like structure with a projected radius of about 100 pc and offset towards positive Galactic longitudes with respect to the dynamical center of the Galaxy (Rodriguez-Fernandez et al. 2006; Molinari et al. 2011). The ring contains the Sgr C, Sgr A (which contains the supermassive black hole marking the center of the Galaxy), Sgr B1, and Sgr B2 star forming complexes. G0.253+0.016 is the most prominent member of a chain of IRDCs at positive Galactic longitudes between Sgr A and Sgr B2 (Lis et al. 2001; Longmore et al. 2013). Longmore et al. (2012) and Rathborne et al. (2014b) found that G0.253+0.016 exhibits a line-width near zero intensity of about ∼50 to 60 km s^{-1}, and an internal velocity dispersion of at least 16 km s^{-1} typical for CMZ clouds that implies a crossing time of about 0.17 Myr.

Models of orbits in barred, tri-axial potentials indicate that gas in the inner CMZ is likely to be moving on x_2 orbits elongated along the minor axis of the bar (Contopoulos & Papayannopoulos 1980; Athanassoula 1992a,b). The major axis of the bar is oriented between 20 and 45 degrees with respect to our line of sight (Binney et al. 1991; Rodriguez-Fernandez & Combes 2008). G0.253+0.016 is located at a projected distance of about 50 pc from Sgr A and has a radial velocity V$_{LSR} \approx$ 40 km s^{-1}. Assuming that it is moving close to the plane of the sky with a velocity of about 150 to 180 km s^{-1} along an elongated x_2 orbit (this is the speed expected for a circular orbit given the enclosed mass), it would have passed near Sgr A about 0.25 to 0.3 Myr ago (Kruijssen et al. 2014). Clouds injected onto x_2 orbits near apocenter with velocities lower than the circular orbit speed at that location

tend to plunge deeper into the potential well. Following pericenter passage near Sgr A, they climb out of the potential to a second apocenter located on the opposite side of the nucleus, and on the opposite side of the Galaxy from the first apocenter. Such plunging, elongated orbits precess at rates which depend on the details of the enclosed mass distribution and orbit eccentricity. Longmore et al. (2013) proposed that the encounter of G0.253+0.016 with Sgr A may have compressed this cloud.

In this paper, high-angular resolution, high dynamic range, and sensitive ALMA observations of J = 1−0 HCO$^+$ are presented that reveal an extensive network of filaments seen in absorption toward G0.253+0.016. The most prominent filament (Figure 1) has an absorption line-width of over 30 km s^{-1} and is nearly parallel to the bright, non-thermal radio filaments which cross the Galactic plane at longitude 0.18° a few arc minutes from G0.253+0.016. Dozens of filaments with less than 20 km s^{-1} linewidths are predominantly seen on the blueshifted side of the HCO$^+$ emission from G0.253+0.016. In this paper, it is shown that these absorption features are produced by very low-density, sub-thermally excited HCO$^+$ absorbing optically thick, but nevertheless subthermaly excited background HCO$^+$ emission from this cloud. If located on the near surface of G0.253+0.016, their blueshifted velocities with respect to the background HCO$^+$ emission would indicate that the cloud surface layers are expanding, contrary to the naive expectation of global collapse if it were a progenitor to a massive cluster.

2. Observations

Observations presented here were obtained with the Atacama Large Millimeter Array (ALMA) located on the Chajnantor plateau in the Northern Chilean Andes. Full details of the observations and data reduction will be presented in another paper (Rathborne et al. 2014a). A short summary is presented below.

G0.253+0.016 was imaged in the 3 mm wavelength bands (ALMA band 3) using 25 of ALMA's 12-meter diameter antennas. The synthesized beam produced by ALMA at this frequency has a diameter of 1.7″ corresponding to a linear scale of 0.07 pc at the 8.5 kpc distance of the CMZ. Because the primary-beam field-of-view of ALMA is small ($\sim$ 70″) and G0.253+0.016 subtends a 1′ by 3′ region, a mosaic consisting of 13 separate pointings was required. Baselines ranged from 13 to 455 meters. G0.253+0.016 was imaged on six separate occasions over the period 29 July to 1 August 2012. Each data set was independently calibrated prior to merging. The ALMA correlator was configured to measure the continuum in a 1.875 GHz bandpass, and to observe 10 different molecular emission lines with a resolution of 0.488 MHz (about 1.5 km s^{-1} velocity resolution) covering a velocity

range from about V_{LSR} = -200 km s^{-1} to about +240 km s^{-1}. Single-dish observations of G0.253+0.016 in the same transitions as observed with ALMA were obtained with the 22 meter Mopra radio telescope in Australia as part of the MALT90 Survey (Foster et al. 2011; Jackson et al. 2013; Foster et al. 2013). The resulting maps were used to restore 0-spacings in the ALMA data in the Fourier domain (Rathborne et al. 2014a).

Final data cubes were gridded to a pixel scale of 0.35″ per pixel. Because the flux in adjacent channels in the data is correlated, the data were re-sampled to 3.4 km s^{-1} per channel. The rms noise in each frequency channel is about 5 mJy (0.26 K) in the 1.7″ beam. At the rest frequency of the HCO$^+$ J = 1-0 transition (89.1885 GHz) a flux of 1 Jy in the 1.7″ diameter beam (or a surface brightness of 1 Jy/beam) corresponds to a brightness temperature of 53.5 K. All temperatures and fluxes refer to values above the cosmic microwave background or any other smooth background which are resolved out by ALMA and removed from the single-dish observations by beam-switching.

3. Results

The blueshifted emission in HCO$^+$ shows an extensive network of curved and linear filamentary structures seen in absorption against the warmer background emission from G0.253+0.016. Figure 1 shows an integrated intensity map of G0.253+0.016 in the J = 1-0 HCO$^+$ transition. While the ALMA HCO$^+$ integrated intensity map is dominated by area-filling emission, the optically thinner H^{13}CO$^+$ cubes show bright arcs resembling bows moving towards increasing R.A. (left in the figures). This overall morphology is also seen in other optically thin (or at least thinner than HCO$^+$) tracers such as HNCO, H$_2$CS, SiO, and SO (Rathborne et al. 2014a).

Figures 2 through 9 show individual 3.4 km s^{-1} wide channel maps in HCO$^+$. The yellow arrows mark the location of a pair of filaments having a length of over $L > 60″$ and a radial velocity dispersion greater than 20 km s^{-1}. Dozens of filaments with line-widths less than 10 to 20 km s^{-1} are located on the blueshifted (low velocity) side of the HCO$^+$ emission. These filaments also have widths of only a few arcseconds, but their lengths tend to be shorter than the broad-line filaments. Some filaments form clusters of nearly parallel strands which at extreme blueshifted radial velocities (V_{LSR} = 5 to 30 km s^{-1}) blend into a complex network of absorption covering most of the spatial extent of G0.253+0.016. The morphology of the absorption filaments do not show any correlation with the underlying filamentary structure of G0.253+0.016 seen in optically thin emission lines. The absorption filaments can be subdivided into two categories based on their observed properties:

Broad-line absorption (BLA) filaments have widths of less than a few arcseconds (< 0.04 to 0.08 pc), lengths of 30 to 50 arcseconds (~ 1 to 2 pc), and absorption profiles extending over a velocity range larger than 20 km s^{-1} around $V_{LSR} = 10$ to 40 km s^{-1}. The two most evident BLAs (marked by in Figures 1 through 9) are nearly parallel to the nearby G0.18 non-thermal filaments seen in 20 and 6 cm wavelength radio continuum images of Yusef-Zadeh et al. (2004). These BLAs have position angles (measured from North to East) of PA $\sim 125°$ to $140°$, nearly perpendicular to the Galactic plane. The nearby non-thermal filaments have PA $\sim 125°$.

Analysis of spatial-velocity cuts and spectra orthogonal to the most prominent BLA filament in Figure 1 shows that it extends from below 17 km s^{-1} to about 45 km s^{-1} (Figure 10). The intensity in the faintest part of the filament ranges from about 0.17 to greater than 0.8 times the HCO$^+$ intensity in the surrounding region which has a brightness temperature of 3 to 4 K (0.05 to 0.08 Jy/beam). Thus corresponding brightness temperatures at the most opaque portions of the BLA filaments range from ~ 0.5 K (0.01 Jy/beam) at the darkest part of the main BLA to about 2 K (0.04 Jy/beam) at more typical locations. The lowest-opacity occurs near the ends of the major BLA filaments. The deepest absorption occurs at the redshifted end of the feature near $V_{LSR} \approx 37$ km s^{-1} at J2000 $\approx$ 17:46:09.79, $-28:42:03.5$. The mean flux along cross-cuts is about 0.5 times the surrounding cloud flux. Thus, the optical depth of the absorbing gas ranges from ~ 0.2 to about 2 with a mean value of 0.7. The HCO$^+$ BLA filaments have no counterparts in any of the other spectral lines. Specifically, they are not seen in other optically thick species such as HCN.

Narrow-line absorption (NLA) HCO$^+$ filaments, some of which are also seen in absorption in other species with high optical depth such as HCN, have line widths of less than 20 km s^{-1}. Some tend to cluster into filament bundles which taken together have velocity extents up to 20 km s^{-1}. These filaments are mostly located at at $V_{LSR} \sim 10$ to 40 km s^{-1}, blueshifted relative to the median radial velocity of G0.253+0.016.

Table 1 lists several examples of NLA filaments. Near the Northwest portion of the cloud, several arcs form nearly concentric loops with radii of about 6″ and 13″ between V_{LSR} = 11 and 21 km s^{-1} (Figures 2 and 3). NLA1 is a narrow line-width absorption feature about 20″ south of the two BLAs. The NLA2 consists of several parallel east-west strands near the middle of the cloud around δ = -28:42:50 (Figures 5, 6, and 7). NLA 3 is a cluster of bent filaments near the redshifted southern part of G0.253+0.016 around δ = -28:43:00 to - 28:44:00 (Figures 4, 5, and 6). Many NLA filaments blend into broad regions of absorption on the blueshifted, low-radial velocity side of the HCO$^+$ data cube. Figure 11 shows spectra of an NLA filament near the northern side of the NLA3 cluster. Figure 12 shows the HCO$^+$ integrated intensity map of G0.253+0.016 with the locations of the BLA and NLA filaments

with the locations of the features listed in Table 1 marked.

At the extreme blueshifted end of the data cube, the NLA filament network blends into an area-filling absorption. The channel maps between $V_{LSR} = 14$ and 21 km s^{-1} indicate that most of the surface of G0.253+0.016 is covered by NLA filaments. The fractional area covered diminishes toward higher radial velocities. Most NLAs are shorter than the BLAs and many are curved. A few, such as those centered near J2000 = 17:46:10.6, -28:41:55 trace nearly complete circles. Others are partial arcs. The distinction between BLA and NLA filaments is not sharp; they form a continuum with decreasing line-widths and lengths from BLA1 and 2 (Table 1) to the narrower and shorter NLA filaments.

Comparison with the HCN and HNCO data (not shown) indicate that some HCO$^+$ NLAs are also seen as absorption features in these tracers (Figure 13). A few HCO$^+$ NLA segments go into emission where their surroundings are dim in HCN or HNCO such as near the projected edges of the cloud. These filaments are confined to within a few arc-seconds of the cloud's edge, indicating that they may be close to the surface of G0.253+0.016.

The distribution of HCO$^+$ absorption features have no correlation with the underlying structure of G0.253+0.016 seen in other tracers. G0.253+0.016 is filamentary in optically thin emission lines such as H^{13}CN where G0.253+0.016 resembles a bow shock propagating towards the east. Figure 14 shows the optically thin H^{13}CO$^+$ in three broad velocity ranges $V_{LSR} = 10.8$ to 27.8 km s^{-1} (blue), 31.2 to 41.4 km s^{-1} (green), and 44.8 to 61.8 km s^{-1} (red). The east-facing bow shapes are not visible in the optically thick HCO$^+$ (or HCN) data presumably because this emission is area-filling and these tracers only probe cloud structure to the $\tau \approx 1$ surface. The emission-line structure of G0.253+0.016 is discussed in Rathborne et al. (2014a). For reference, Figure 15 shows the 3 mm continuum emission from Rathborne et al. (2014a). It is unclear what fraction of this emission is produced by dust and what fraction is produced by free-free emission.

3.1.   Opacity and Excitation Conditions for HCO$^+$

The typical HCO$^+$ brightness temperature in both the ALMA and single dish observations is only about 2 to 4 K (Rathborne et al. 2014a,b), considerably lower than the gas temperatures of 60 to 80 K inferred from NH$_3$ or H$_2$CO observations (Lis et al. 2001; Mills & Morris 2013; Ao et al. 2013) and even lower than the dust temperature, which has been estimated to be around 19 K in the cloud center and about 27 K at the cloud surface (Lis et al. 2001; Pierce-Price et al. 2000; Longmore et al. 2012). The ALMA data shows that the HCO$^+$ emission is area filling at arcsecond scales. Thus, the low brightness temperature

must be due to low excitation temperature at the $\tau_{12} = 1$ surface, implying densities much lower than the critical density for the J=1−0 89 GHz transition of HCO$^+$ (for which the critical density is $\sim 2 \times 10^5$ cm^{-3}).

Comparison with the H^{13}CO$^+$ ALMA images demonstrates that the HCO$^+$ emission is optically thick at most locations. The area-integrated intensity ratio of HCO$^+$ divided by the area-integrated ratio of H^{13}CO$^+$ is $R_{12/13}$ = I(HCO$^+$)/I(H^{13}CO$^+$) = 10 ± 1 for the northern part of G0.253+0.016 and $R_{12/13} = 11 \pm 1$ for the southern part for integration areas ranging from 0.3 to 2.1 square arc-minutes. The maximum HCO$^+$ brightness (0.23 Jy/beam or 12.3 Kelvin) occurs in a small $3''$ by $8''$ elongated knot near the southern part of G0.253+0.016 at J2000 = 17:46:08.5, −28:43:33 at V$_{LSR}$ = 55 km s^{-1}. At this location, the ratio $R_{12/13} \approx 12$. Thus, the observed brightness ratio, $R_{12/13}$ is lower than the abundance ratio, $X_{12/13} = [^{12}C]/[^{13}C]$.

Langer & Penzias (1990) measured the abundance ratio $X_{12/13}$ as a function of Galactocentric radius finding that in the CMZ $X_{12/13} \approx 24$. In a more recent study, Riquelme et al. (2010) found a similar ratio in most parts of the CMZ. However, near cloud edges, some ratios as high as 40 were found. Milam et al. (2005) found a lower value in the CMZ of $X_{12/13} \approx 17 \pm 7$. Thus, there may a some intrinsic variation possibly do to local enrichments or depletion such as might be caused by local stellar processing and injection into the ISM or isotope-selective photo-dissociation (Röllig & Ossenkopf 2013; Lyons & Young 2005; Bally & Langer 1982).

Assuming that the $X_{12/13}$ is 24 in G0.253+0.016, that the excitation temperatures of H^{13}CO$^+$ and HCO$^+$ are the same, and that for HCO$^+$ the observed brightness is equal to the excitation temperature, as expected for an optically thick emission line, the $R_{12/13}$ ratio of $\sim$10 indicates that the mean emission line optical depth of HCO$^+$ is

$$\tau_{12} \approx X_{12/13} ln[R_{12/13}/(R_{12/13} - 1)] \sim 2.5$$

For $X_{12/13}$ ranging from 17 to 40, τ_{12}, $R_{12/13} = 10$ implies that τ_{12} ranges from 1.5 to 2.5.

In the HCO$^+$ photosphere (where $\tau_{12} \sim 1$), the density must be much lower than the critical density, implying sub-thermal excitation, and densities much lower than the mean density of G0.253+0.016. The brightness temperature of HCO$^+$ implies that $T_{ex} < 10$ K over most of the G0.253+0.016 photosphere. Clark et al. (2013) modeled both the gas and dust temperatures in G0.253+0.016, finding that high gas temperatures and lower dust temperatures can be explained by a very high cosmic-ray flux and ionization rate. The enhanced cosmic-ray flux may also enhance the abundances of certain molecules such as methanol (Yusef-Zadeh et al. 2013) and HCO$^+$.

HCO$^+$ is the most abundant molecular ion next to H$_3^+$ in the molecular phase of

the interstellar medium. Collisional excitation of its J=1-0 transition requires a collision partner density (H_2 and He) of $n > 10^4$ cm^{-3} to thermalize. HCO$^+$ has as relatively high abundance of $n(HCO^+)/n(H_2) \sim 10^{-9}$ to 10^{-7} in nearby molecular clouds. HCO$^+$ is created by the reaction $CO + H_3^+ -> HCO^+ + H_2$ and destroyed by reactions with H_2, $HCO^+ + H_2 -> H_2CO + H^+$ or by recombination with electrons, $HCO^+ + e^- -> CO + H^+$. The large abundance of H_3^+ in the CMZ (Goto et al. 2008, 2011) may drive the HCO$^+$ abundance in the CMZ to values near the upper-end of the above range.

The column densities of the absorption filaments can be estimated from the absorption optical depth. Following Liszt & Lucas (2004) the column density of a linear molecule having dipole moment μ (about 4 Debye for HCO$^+$) absorbing from its ground state is

$$N_0 = \frac{8.0 \times 10^{12} \int \tau_{10} dV}{\mu^2 (1 - exp(-h\nu_{10}/kT_{ex}))}$$

where ν_{10} is the J $= 1-0$ frequency (89.1885 GHz) for HCO$^+$ and T_{ex} is the excitation temperature. Measuring the HCO$^+$ fluxed in the filament and comparing this with the surrounding off-filament pixels indicates that typically about one-half of the background light is absorbed, implying a typical absorption optical depth of about 0.7. For the broad-line filaments, $dV \sim 10$ to 30 km s^{-1} and $\tau_{10} \sim 0.2$ to 2 with a mean value of 0.7. For a typical equivalent width (integral of absorption optical depth over the line width) of 10 km s^{-1}, the column density of HCO$^+$ absorbers is $N_0 \approx 10^{13}$ cm^{-2} for $T_{ex} = 2.73$ K, and 6×10^{13} cm^{-2} for $T_{ex} = 10$ K.

Table 2 lists the excitation temperatures (T_{ex}), opacities (τ), and brightness temperatures (T_R) for the J $= 1-0$ transition of HCO$^+$ for a range of molecular hydrogen volume densities (n) and HCO$^+$ column densities (N) using the radiative transfer code RADEX (van der Tak et al. 2007). These calculations show that an H_2 density of 1×10^3 cm^{-3} an HCO$^+$ column density of $1 - 10 \times 10^{13}$ cm^{-2} and line width $\Delta V = 10$ km s^{-1} in a gas with a kinetic temperature of 60 K results in an excitation temperature of about $2.8 - 3.2$ K, an optical depth $0.8 - 7$ in the J $= 1$-0 line. These parameters would produce the absorption seen in the NLA filaments. The BLA filaments require a slightly lower H_2 density to produce the low observed brightness temperature and an opacity of order unity required to explain the amount of background attenuation. The HCO$^+$ radiation field of G0.253+0.016 may contribute to the excitation of the upper state by effectively raising the background radiation temperature (radiative pumping). Detailed modeling of the excitation conditions and radiative transfer using realistic cloud geometries is needed to determine if the low observed brightness temperature of the NLA and BLA filaments can be used to place a lower bound on separation between the absorbing gas and G0.253+0.016.

The width of these filaments is less than about 2$''$ or about 0.08 pc. (If only 1$''$ wide,

the filaments must be completely dark and only a lower bound can be placed on their optical depth. Higher angular resolution ALMA observations will be obtained during ALMA Cycle 1 to measure their actual widths.) From the estimated column density and HCO^+ abundance $X(HCO^+) = 10^{-7}$, assuming that the depth of the filament is comparable to its projected width, the higher excitation temperature ($T_{ex} = 10$ K) would imply an H_2 column density of 6×10^{20} cm^{-2} and a volume density of around 2.5 to 5×10^3 cm^{-3}. A density larger than this value would drive the absorption filaments into emission in HCO^+. A lower HCO^+ abundance increases the estimated volume density proportionally and conversely, a higher HCO^+ abundance decreases the H_2 volume density. Thus, either the HCO^+ abundance must be higher than $X(HCO^+) = 10^{-7}$, or the line-of-sight depth of the filaments must be larger than their projected widths.

It is possible that the filaments are sheets seen edge-on so that the line-of-sight depth is much larger than projected width of the filament. In such a sheet, the column density to volume density ratio can be much larger than for a cylinder. For a given HCO^+ abundance, the observed column density requires a volume density that is lower by the ratio of the line-of-sight depth of the sheet divided by its projected width on the plane of the sky. Such edge-on sheets may be produced by shocks propagating into molecular media at right angles to our line-of-sight. With $n(H_2) < 5 \times 10^3$ cm^{-3}, the densities in the absorption filaments must be lower than the density at the $\tau \sim 1$ surface in HCO^+ which is sub-thermally excited, and well below the mean density of G0.253+0.016, $n(H_2) \approx 7 \times 10^4$ cm^{-3} (Lis et al. 2001; Longmore et al. 2012; Rathborne et al. 2014b).

Inspection of the HCO^+ and HCN data show that both tracers are heavily absorbed on the blueshifted, approaching side of the spectral line profiles. Thus, there is a pervasive layer of sub-thermally excited, low density HCO^+ and HCN bearing gas in front of G0.253+0.016. If associated with G0.253+0.016, this gas would indicate the presence of an extended layer expanding from G0.253+0.016 at velocities 10 to 20 km s^{-1} over the entire face of this cloud.

While NLA filaments near $V_{LSR} = 0$ km s^{-1} could be located anywhere between the Sun and G0.253+0.016, the higher radial velocity NLA filaments with $V_{LSR} > 10$ km s^{-1} are most likely to be in the CMZ (local gas is found between $V_{LSR} \sim -10$ to $+10$ km s^{-1} and the Galactic spiral arms between the Sun and the CMZ are at $V_{LSR} \sim -10$ to -65 km s^{-1}). Near the projected edge of G0.253+0.016 some NLA filaments go faintly into emission in HCN and HNCO. Because these features disappear a few arc seconds beyond the cloud's edge, they must be physically close to G0.253+0.016, suggesting that they trace sub-thermal HCO^+ and HCN molecules on the near surface of the cloud.

4. The Dynamic State of G0.253+0.016: Collapse, Expansion, or Both?

Rathborne et al. (2014b) analyzed millimeter and sub-millimeter-wave emission in multiple transitions from G0.253+0.016 obtained with the Mopra and APEX single-dish telescopes. In addition to the large north-south velocity gradient they found that the optically thick dense-gas tracers were systematically redshifted with respect to the optically thin and hot gas tracers, indicating radial motions which could be interpreted as either due to expansion or collapse. If the brighter, redshifted emission in optically thick species such as HCO^+ and HCN originate in an externally-heated layer at the *front surface*, then the cloud is contracting. Rathborne et al. (2014b) refer to this as their 'Baked Alaska' model. The bright blueshifted emission expected from the far-side heated layer would be absorbed by HCO^+ molecules in the supersonically turbulent, colder, cloud interior. This interpretation requires that the excitation temperature of the HCO^+ J=1−0 transition in the cloud surface layer producing the redshifted line component must be higher than excitation temperature of the component producing the lower-velocity and lower brightness-temperature emission in the cloud interior. Alternatively, if the excitation temperature in the layer where the optical depths reach a value of order unity is low compared to the excitation temperature deep in the cloud interior, then these observations can be interpreted as evidence for expansion of the cloud surface layers. For sub-thermal excitation of molecules at the cloud surface, collapse would produce redshifted absorption while expansion would produce blueshifted absorption.

At lower, blueshifted radial velocities, the HCO^+ J=1−0 transition is seen as a network of absorption filaments against brighter background emission. The brighter, background HCO^+ emission appears to fill the synthesized ALMA beam and to cover most of the projected surface area of G0.253+0.016 with a peak brightness temperature of order 2 to at most 10 K, well below the gas kinetic temperature, $T_K > 60$ K. A peak line temperature lower than T_K requires that either the emitting region fills only a small portion of the telescope beam ('beam dilution'), or a small fraction of the spectral channel ('frequency dilution'), or that the excitation temperature T_{ex} at the $\tau \approx 1$ surface be much lower than T_K. The bright HCO^+ emission between the absorption filaments appears smooth on scales larger than the 1.7″ ALMA beam, and continuous from one velocity channel to the next, indicating that beam and frequency dilution of the HCO^+ emission is unlikely. Thus, the relatively low brightness temperature of HCO^+ is most likely due to low excitation temperature, implying that the H_2 density near the $\tau = 1$ surface is much lower than the critical density for the HCO^+ J $= 1−0$ transition.

The HCO^+ filaments are seen in absorption against this background emission, they have an even lower excitation temperature than the regions seen in emission. If these blueshifted features are at the cloud surface, the G0.253+0.016 surface layers must be expanding away

from the cloud center of mass despite the large mass and gravity field. This is consistent with the second ('P-Cygni') interpretation of the single-dish data presented by Rathborne et al. (2014b).

The mass-loss rate is difficult to estimate because the density on the absorbing layer is an upper bound, the column density is a lower-bound (based on an assumed HCO^+ abundance), and the thickness of the absorbing layer is not known. For a given density $n(H_2)$, and assuming that all sides of the cloud are expanding in a manner similar to that side facing the Sun, the mass-loss rate is given by $\dot{M} \sim 4\pi f R_{eff}^2 \mu m_H n(H_2) V$ where f is the fraction of the cloud surface area occupied by expanding gas, $R_{eff} \approx 2.7$ pc is the mean cloud radius, $n(H_2)$ is the area averaged mean density of the NLA filaments at the cloud's surface, and $V \sim 10$ to 20 km s^{-1} is the expansion speed of the absorbing layer. For $f = 0.5$ and $n(H_2) = 10^3$ cm^{-3}, set by the constraint that HCO^+ in the absorbing gas is severely sub-thermally excited, $\dot{M} \sim 0.03$ to 0.06 M$_\odot$ yr^{-1}. In the last 0.25 Myr, since its close passage to Sgr A, G0.253+0.016 could have lost 10 to 20% of its mass.

It is possible that G0.253+0.016 is simultaneously undergoing *both* collapse and expansion. The presence of a maser and at least one massive clump surrounding it suggests that at least one moderate or high mass star is forming in the cloud interior. The cold and dense cloud interior may thus be experiencing gravitational collapse and star formation. However, the lack of internal heating and absence of any other signposts of young stars other than the maser source, suggests that the cloud is only in the earliest phases of star formation. Blueshifted absorption in optically thick species such as HCO^+ over much of the cloud surface area is an indication that outer layers may be expanding.

5. Discussion

The filamentary structure of molecular clouds has been recognized for decades (Bally et al. 1987a). However, the extensive arc-second scale HCO^+ absorption filaments revealed by ALMA are new. The broad-line (BLA) filaments in G0.253+0.016 are extraordinary because of their narrow minor axis dimension (less than $\sim 10^4$ AU), their 20 km s^{-1} width in absorption, and their low antenna temperatures. The more abundant narrow-line (NLA) filaments are less extreme in their velocity extent. Comparison of the optically thick HCO^+ and HCN cubes with the other ALMA spectral line cubes of optically thinner tracers such as HNCO, SiO, C_2H, H_2CS, $H^{13}CN$, and $H^{13}CO^+$ show that HCO^+ and HCN are heavily absorbed between $V_{LSR} = -2.8$ and about $+30$ km s^{-1}. The BLAs are only seen in HCO^+ and have no corresponding features in any other species in either emission or absorption.

Two models are considered for the BLA filaments. The BLAs may be associated with dense gas in the Galactic Center Ring (GCR) a portion of which has a radial velocity V_{LSR} = 10 to 30 km s^{-1} towards Galactic longitude of 0.18 (Rodriguez-Fernandez et al. 2006; Rodriguez-Fernandez & Combes 2008). Assuming that the GCR has similar orientation and kinematics but is larger than the 100 pc radius ring proposed by Molinari et al. (2011), the front side is expected to have positive radial velocities while the far side is expected to have negative velocities. Given the possible association of G0.253+0.016 with the Molinari ring, the front-side of GCR may be in front of G0.253+0.016. Low density, low-excitation gas could then be seen in absorption against the warmer emission from the cloud. In this scenario the BLAs are produced by sub-thermal HCO$^+$ far in front (a few to as much as ~200 pc in front of G0.253+0.016). Their narrow widths, highly supersonic velocity extents, and elongated filamentary morphology suggest that they are ram pressure confined. In this model, they may be caustic surfaces produced where shock fronts are moving in the plane of the sky and whose post-shock layers are sheets observed very close to edge-on. Thus, their depth along the line-of-sight may be much larger than their observed widths. The HCO$^+$ molecules must either survive passage through the shock, or are rapidly formed in the post-shock cooling layers. The crossing time of these filaments is about 10^3 years. If molecule reformation is responsible for the HCO$^+$ abundance, then this time-scale establishes a limit on the formation time.

The alternative model is that the BLAs are related to the non-thermal filaments near Galactic longitude 0.18 and are magnetically confined. This picture is motivated by the similar orientations of the BLAs and the 20-cm non-thermal filaments that lie only a few parsecs in projection from the southeast edge of G0.253+0.016. Both sets of filaments are oriented roughly at right angles to the Galactic plane. Using equipartition arguments applied to the synchrotron, Yusef-Zadeh & Morris (1987) estimated that the magnetic fields in the non-thermal streamers have strengths of about 0.05 to 0.2 milli-Gauss.

The polarization of the dust continuum emission from G0.253+0.016 has been measured at λ = 350 μm (Dotson et al. 2010). The magnetic field is nominally orthogonal to the 350 μm polarization vector. Inspection of Figure 39 in Dotson et al. (2010) shows that the magnetic field in the cloud interior where most of the sub-mm dust emission originates, closely follows the bow-shaped emission-line filaments observed in the optically-thin tracers. The magnetic field in the northern part of G0.253+0.016 is approximately orthogonal to the Galactic plane and parallel to the BLA filaments. The magnetic field in the southern part of G0.253+0.016 is roughly aligned with the Galactic plane.

Application of the Chandrasekhar-Fermi method to estimating magnetic field strengths in the molecular gas in the CMZ as traced by sub-millimeter polarimetry of the dust con-

tinuum emission leads to field strength estimates of 1 - 3 milli-Gauss (Chuss et al. 2003). Using the scaling relations of magnetic field strength with cloud density based on Zeeman effect measurements (Crutcher 2012) and assuming a mean cloud density of few $\times 10^5$ cm^{-3} leads to similar field strength estimates. Ferrière (2010) presented a review of CMZ magnetic fields.

An ionization fraction of $\sim 10^{-7}$ (the estimated abundance of HCO$^+$ in the absorbing medium) implies very long ambipolar diffusion time-scales and highly elongated structures if magnetic fields are present in the absorption region. Heavy molecular ions such as HCO$^+$ gyrate around the magnetic field lines at a frequency $f_{gyro} \sim eB/m(HCO^+)c \approx 0.3\ B_{mG}$ radians per second. Here, e is the electron charge, c is the speed of light, $m_{HCO+} = 29\ m_H$ is the mass of an HCO$^+$ molecule, and B_{mG} is the magnetic field in units of 1 milli-Gauss. Using the observed spectral line half-width of the most prominent BLA filament, $\Delta V \sim 10$ km s^{-1}, implies a gyro-radius of HCO$^+$ molecules of ~ 30 km. The mean-free path of molecules, $\lambda_{mfp} \sim 1/n(H_2)\sigma$ for a density $n(H_2) = 10^3$ and a collision cross-section $\sigma \sim 10^{-15}$ cm^{-2} is $\lambda_{mfp} \sim 10^{12}$ cm, 5-orders of magnitude smaller than the width of the BLA filaments ($\sim 10^{17}$ cm). The mean time between molecular collisions which lead to diffusion is $t_{col} \sim 10^6$ seconds. To random-walk a distance 10^5 times larger than the mean free-path requires about 10^{10} collisions. Thus, the time for molecules to diffuse over a distance of $r_{filament} \sim 10^4$ AU (the typical width of the absorption filaments) is therefore $t_{AD} \sim 10^{10} t_{col} \sim 10^{16}$ seconds. For the parameters implied by the observations, the magnetic field and the partially ionized molecular gas are tightly coupled. The effective diffusion velocity *across* the filaments is $V_{perp} \sim r_{filament}/t_{AD} \sim 10$ cm s^{-1}. However, atoms and molecules can move unimpeded *along* the field lines at the $\Delta V \sim 10$ km s^{-1} measured velocity dispersion. Thus the aspect ratio (length-to-width) of magnetized filaments can be as high as $\Delta V/V_{perp} > 10^5$.

5.1. Expansion of the Surface G0.253+0.016: Photo-ablation?

Two mechanisms could be responsible for the apparent expansion of the near-side surface layers of G0.253+0.016; photo-ablation and stored magnetic energy. The first mechanism relies on external heating of the cloud surface layers by the combined effects of UV, soft X-ray, visual, and near-IR radiation that can photo-ablate cloud surfaces, generate large internal motions, and generate shocks which compress the cloud surface layers (Mellema et al. 2006; Henney et al. 2009; Arthur et al. 2011). Diffuse dust emitting between 8 and 70 μm tends to be associated with photo-ionized plasmas in HII regions. The extended 20 cm free-free continuum (Yusefzadeh et al. 2004) and 8 to 70 μm continuum emitted by diffuse mid-IR emission from warm dust implies that much of the inner 100 pc of the Galaxy

contains photo-ionized plasma and warm dust, likely produced by radiation from massive stars. Although the Spitzer and WISE mid-IR images show that the Galactic Center Bubble located between Sgr A and G0.253+0.016, and likely ionized and heated by the Arches and Quintuplet clusters, dominates the diffuse mid-IR emission in the CMZ, these images also exhibit somewhat fainter and more diffuse warm dust emission centered about 6′ (15 pc in projection) due East of G0.253+0.016 at $[l, b] = [0.304, -0.067]$ (J2000 = 17:46:36.2, -28:42:41).

Diffuse 20 cm radio continuum and several HII regions within 6′ of this region of peak infrared emission (but generally due East of G0.253+0.016) indicate the presence of OB stars whose energy output may irradiate and heat the G0.253+0.01 cloud's surface. If the Lyman continuum luminosity of these stars is $Q_{50} \sim 10^{50}$ ionizing photons per second, and located at a distance $D_{15} = 15$ pc, the electron density at the surface of G0.253+0.016 would be (neglecting any intervening extinction) about $n_e = (Q/4\pi\alpha_B r)^{1/2}D^{-1} \sim 40 \ Q_{50}^{1/2} r_3^{-1/2} D_{15}^{-1}$ cm^{-3} assuming a spherical cloud of radius $r = r_3 \sim 3$ pc (here, $\alpha_B = 2.6 \times 10^{-13}$ cm^3 s^{-1} is the Case B hydrogen recombination coefficient). But, G0.253+0.016 appears filamentary with local radii of curvature at least an order of magnitude smaller in at least one direction. Thus, the actual electron density may be $n_e > 10^2$ cm^{-3}. The implied mass-loss rate due to heating (assuming that the gas is accelerated to about the sound-speed in ionized gas; ~ 10 km s^{-1}) is about 10^{-3} M$_\odot$ yr^{-1} or only about 10^2 to 10^3 M$_\odot$ in 0.25 Myr. This is an order-of-magnitude lower than the mass-loss rate estimated from the NLA absorption filaments. Unless additional energy input mechanisms operate, photo-ablation is an unlikely source of cloud surface layer expansion.

5.2. Expansion of the Surface G0.253+0.016: Magnetic Bounce?

Longmore et al. (2013) proposed that G0.253+0.016 passed near Sgr A about 0.25 Myr ago. Passage of the cloud through the deepest part of the Galactic gravitational potential would have compressed the cloud. If its interior magnetic fields were sufficiently tangled, they would act as a spring, storing the energy of compression, limiting the dissipation of internal motions by shocks. As G0.253+0.016 emerged from the potential well, the compressed fields could drive re-expansion of the cloud. While some regions with high density or mass-to-flux ratios may collapse, less dense or relatively weakly bound parts of the cloud such as its outer layers, may expand as the fields relax.

An order of magnitude estimate of the mean field strength required to support such a 'bounce' can be obtained by assuming that the stored magnetic energy, $E_B \sim fB^2r^3$ is comparable to the gravitational self-energy $E_G \sim gGM^2/r$. Here, f and g are factors of order

unity depending on the magnetic field geometry, the cloud shape, and density distribution, and for G0.253+0.016, $r \sim 3$ pc is the mean cloud radius, and $M \sim 10^5$ M$_\odot$ is the cloud mass. If the gravitational potential energy is similar to the magnetic energy (as required by a 'bounce'), these parameters imply a mean magnetic field strength $B \sim 1.5$ milli Gauss, consistent with the magnetic field-strength estimates. Thus, the adiabatic behavior of a tangled internal magnetic field could drive a re-expansion of G0.253+0.016 following its emergence form the deepest part of the Galactic gravitational potential.

Future work should search for evidence for BLAs in other optically-thick ground-state transitions of ions such as N$_2$H$^+$. BLAs detected only in other ions would lend support to the magnetic structure interpretation. BLAs detected in other neutral species, especially ones with enhanced abundances in shocks, would provide support for the shock-wave interpretation. High resolution dust continuum polarization measurements and searches for Zeeman splitting are needed to constrain the magnetic field geometry and strength to determine if the magnetic flux-to-mass ratio is super-critical and allows the cloud to collapse, or sub-critical and may prevent collapse and formation of a cluster of stars.

6. Conclusions

ALMA Cycle 0 observations of the massive, compact, and dense Galactic center cloud, G0.253+0.016 are presented with an angular resolution of about 1.7″ in the HCO$^+$ and H^{13}CO$^+$ J $= 1-0$ lines. The main results derived from these observations are:

[1] The observed intensity ratios of HCO$^+$ and H^{13}CO$^+$ indicate that the mean optical depth of HCO$^+$ is around unity or higher. The observed J$=1-0$ HCO$^+$ brightness temperature of 2 to 12K in a cloud in which the kinetic temperature of the gas is estimated to be around 60 to 80 K indicates sub-thermal excitation at the HCO$^+$ photosphere and an H$_2$ density (n(H$_2$) $\sim 10^3$ cm^{-3}) more than an order of magnitude lower than the critical density for the J$=1-0$ transition and more than an order of magnitude lower than the mean density of G0.253+0.016.

[2] The ALMA observations reveal a network of blueshifted (relative to the cloud) absorption filaments seen against the sub-thermally excited HCO$^+$ emission. These filaments must have densities even lower than density at the $\tau_{12} \sim 1$ photosphere where most of the HCO$^+$ emission is produced. A few broad-line absorption (BLA) filaments have line widths of over 20 km s^{-1}, widths of only a few arc seconds, and lengths of nearly 1 arc minute. They are only seen in HCO$^+$. The BLA filaments may be foreground magnetic structures possibly associated with the brightest non-thermal filaments that cross the Galactic plane at

longitude 0.18°. Alternatively, they may be shock fronts in foreground CMZ clouds propagating orthogonal to the line-of-sight so that their compressed layers are seen nearly edge-on with a depth along the line-of-sight much greater than their projected widths. Additionally, G0.253+0.016 is laced with dozens of narrow-line absorption (NLA) filaments with line widths of less than 20 km s^{-1}. Most of these features are seen on the blueshifted side of the line profiles. A few have counterparts in HCN. Some absorption filaments seen in both HCO$^+$ and HCN which extend over faint HCN backgrounds go into emission in HCN but not in HCO$^+$. HCN also shows extensive absorption on the blueshifted side of G0.253+0.016. These characteristics suggest that the NLA filaments trace sub-thermally excited, optically thick gas on the front surface of G0.253+0.016.

[3] The blueshift of the absorption filaments relative to the peak HCO$^+$ emission indicates that the surface layers of G0.253+0.016 are expanding with velocities larger than 5 to 20 km s^{-1} with respect to the cloud's center of mass. The apparent "P-Cygni" line profile may be an indication of re-expansion of the G0.253+0.016 surface layers following a recent passage close to Sgr A. Compression of a milli-Gauss magnetic field during the passage, followed by subsequent expansion driven by stored magnetic energy may be responsible.

[4] Weather or not G0.253+0.016 will form a star cluster or only a few stars remains unclear. Although the HCO$^+$ absorption indicates that the cloud surface layers are expanding, the cloud interior may be in the earliest stages of star formation as indicated by the presence of at least one cloud core with an associated water maser. The dynamic state of the dozens of other 3 mm dust condensations in G0.253+0.016 remains unclear. Measurements of the amplitude and geometry of the magnetic field are needed to determine if the magnetic pressure is sufficient or insufficient to prevent this massive, high-density, and compact cloud from collapsing to form a cluster or association of stars.

REFERENCES

Ao, Y. et al. 2013, A&A, 550, A135

Arendt, R. G. et al. 2008, ApJ, 682, 384

Arthur, S. J., Henney, W. J., Mellema, G., de Colle, F., & Vázquez-Semadeni, E. 2011, MNRAS, 414, 1747

Athanassoula, E. 1992a, MNRAS, 259, 328

—. 1992b, MNRAS, 259, 345

Bally, J. & Langer, W. D. 1982, ApJ, 255, 143

Bally, J., Langer, W. D., Stark, A. A., & Wilson, R. W. 1987a, ApJ, 312, L45

Bally, J., Stark, A. A., Wilson, R. W., & Henkel, C. 1987b, ApJS, 65, 13

—. 1988, ApJ, 324, 223

Binney, J., Gerhard, O. E., Stark, A. A., Bally, J., & Uchida, K. I. 1991, MNRAS, 252, 210

Breen, S. L. & Ellingsen, S. P. 2011, MNRAS, 416, 178

Chuss, D. T., Davidson, J. A., Dotson, J. L., Dowell, C. D., Hildebrand, R. H., Novak, G., & Vaillancourt, J. E. 2003, ApJ, 599, 1116

Clark, P. C., Glover, S. C. O., Ragan, S. E., Shetty, R., & Klessen, R. S. 2013, ApJ, 768, L34

Contopoulos, G. & Papayannopoulos, T. 1980, A&A, 92, 33

Crutcher, R. M. 2012, ARA&A, 50, 29

Dotson, J. L., Vaillancourt, J. E., Kirby, L., Dowell, C. D., Hildebrand, R. H., & Davidson, J. A. 2010, ApJS, 186, 406

Ferrière, K. 2010, Astronomische Nachrichten, 331, 27

Ferrière, K., Gillard, W., & Jean, P. 2007, A&A, 467, 611

Figer, D. F. et al. 2002, ApJ, 581, 258

Foster, J. B. et al. 2011, ApJS, 197, 25

—. 2013, PASA, 30, 38

Goto, M., Usuda, T., Geballe, T. R., Indriolo, N., McCall, B. J., Henning, T., & Oka, T. 2011, PASJ, 63, L13

Goto, M. et al. 2008, ApJ, 688, 306

Habibi, M., Stolte, A., Brandner, W., Hußmann, B., & Motohara, K. 2013, A&A, 556, A26

Henney, W. J., Arthur, S. J., de Colle, F., & Mellema, G. 2009, MNRAS, 398, 157

Higuchi, A. E., Chibueze, J. O., Habe, A., Takahira, K., & Takano, S. 2014, AJ, 147, 141

Jackson, J. M. et al. 2013, PASA, 30, 57

Kauffmann, J., Pillai, T., & Zhang, Q. 2013, ApJ, 765, L35

Kruijssen, J. M. D., Longmore, S. N., & Dale, J. E. 2014, in preparation

Langer, W. D. & Penzias, A. A. 1990, ApJ, 357, 477

Lis, D. C. & Carlstrom, J. E. 1994, ApJ, 424, 189

Lis, D. C. & Menten, K. M. 1998, ApJ, 507, 794

Lis, D. C., Menten, K. M., Serabyn, E., & Zylka, R. 1994, ApJ, 423, L39

Lis, D. C., Serabyn, E., Zylka, R., & Li, Y. 2001, ApJ, 550, 761

Liszt, H. & Lucas, R. 2004, A&A, 428, 445

Longmore, S. N. et al. 2013, MNRAS, 433, L15

—. 2012, ApJ, 746, 117

Lyons, J. R. & Young, E. D. 2005, Nature, 435, 317

Mellema, G., Arthur, S. J., Henney, W. J., Iliev, I. T., & Shapiro, P. R. 2006, ApJ, 647, 397

Menten, K. M., Pillai, T., & Wyrowski, F. 2005, in IAU Symposium, Vol. 227, Massive Star Birth: A Crossroads of Astrophysics, ed. R. Cesaroni, M. Felli, E. Churchwell, & M. Walmsley, 23–34

Milam, S. N., Savage, C., Brewster, M. A., Ziurys, L. M., & Wyckoff, S. 2005, ApJ, 634, 1126

Mills, E. A. C. & Morris, M. R. 2013, ApJ, 772, 105

Molinari, S. et al. 2011, ApJ, 735, L33

—. 2010a, A&A, 518, L100

—. 2010b, PASP, 122, 314

Morris, M. & Serabyn, E. 1996, ARA&A, 34, 645

Pierce-Price, D. et al. 2000, ApJ, 545, L121

Portegies-Zwart, S. F., McMillan, S. L. W., & Gieles, M. 2010, ARA&A, 48, 431

Ramírez, S. V., Arendt, R. G., Sellgren, K., Stolovy, S. R., Cotera, A., Smith, H. A., & Yusef-Zadeh, F. 2008, ApJS, 175, 147

Rathborne, J. M. et al. 2014a, ApJ, submitted

—. 2014b, ApJ, 786, 140

Riquelme, D., Amo-Baladrón, M. A., Martín-Pintado, J., Mauersberger, R., Martín, S., & Bronfman, L. 2010, A&A, 523, A51

Rodriguez-Fernandez, N. J. & Combes, F. 2008, A&A, 489, 115

Rodriguez-Fernandez, N. J., Combes, F., Martin-Pintado, J., Wilson, T. L., & Apponi, A. 2006, A&A, 455, 963

Röllig, M. & Ossenkopf, V. 2013, A&A, 550, A56

van der Tak, F. F. S., Black, J. H., Schöier, F. L., Jansen, D. J., & van Dishoeck, E. F. 2007, A&A, 468, 627

Yusef-Zadeh, F., Cotton, W., Viti, S., Wardle, M., & Royster, M. 2013, ApJ, 764, L19

Yusef-Zadeh, F., Hewitt, J. W., & Cotton, W. 2004, ApJS, 155, 421

Yusef-Zadeh, F. & Morris, M. 1987, ApJ, 322, 721

Yusefzadeh, F., Hewitt, J. W., & Cotton, W. 2004, ApJS, 155, 421
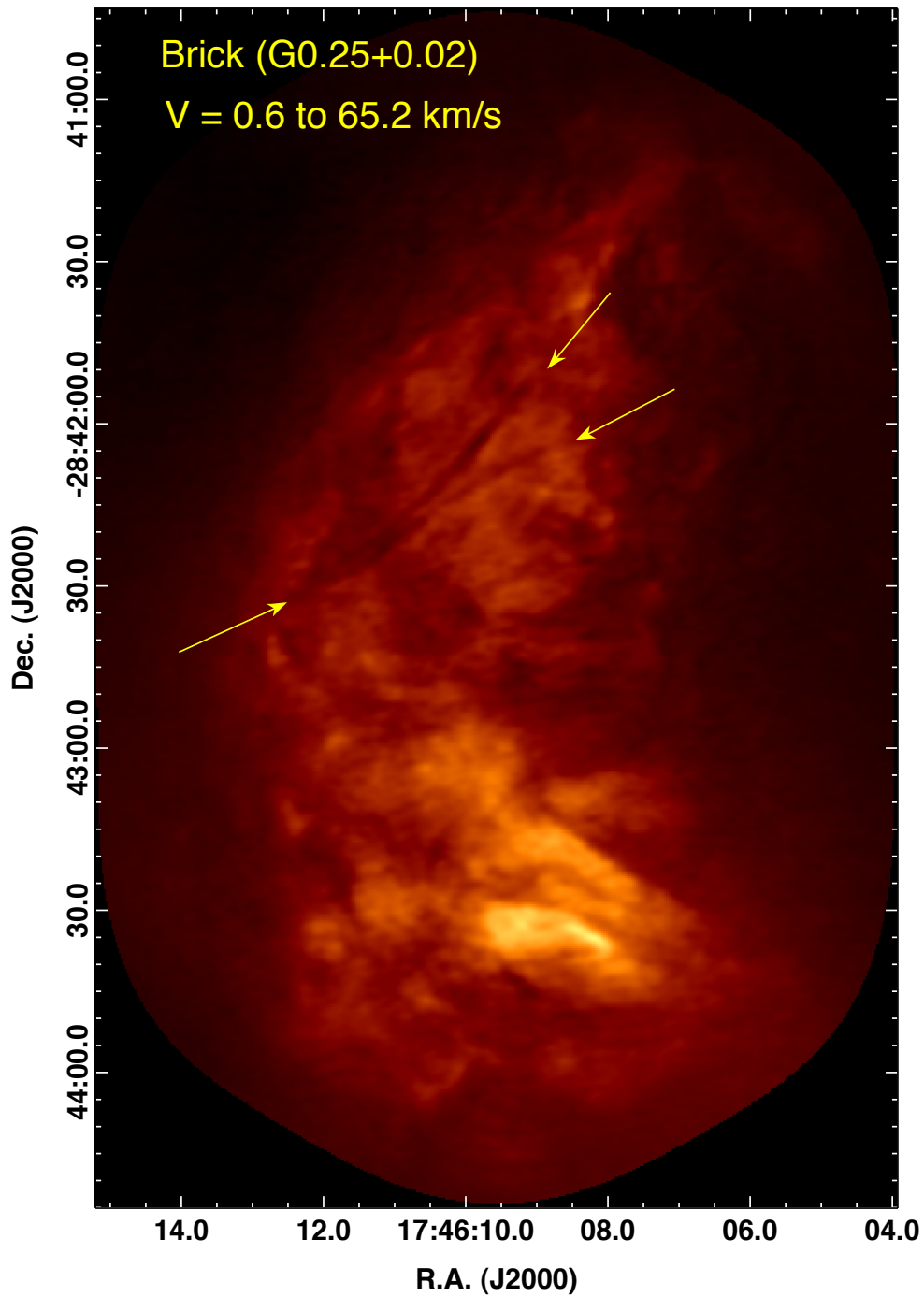
Fig. 1.— A velocity integrated image shoving G0.253+0.016 in the HCO$^+$ J = 1−0 transition. The velocity range extends from V$_{LSR}$ = 0.6 km s^{-1} to 65.2 km s^{-1}. Arrows mark the locations of the two broad line absorption (BLA) filaments. These arrows are retained in Figures 2 through 9.
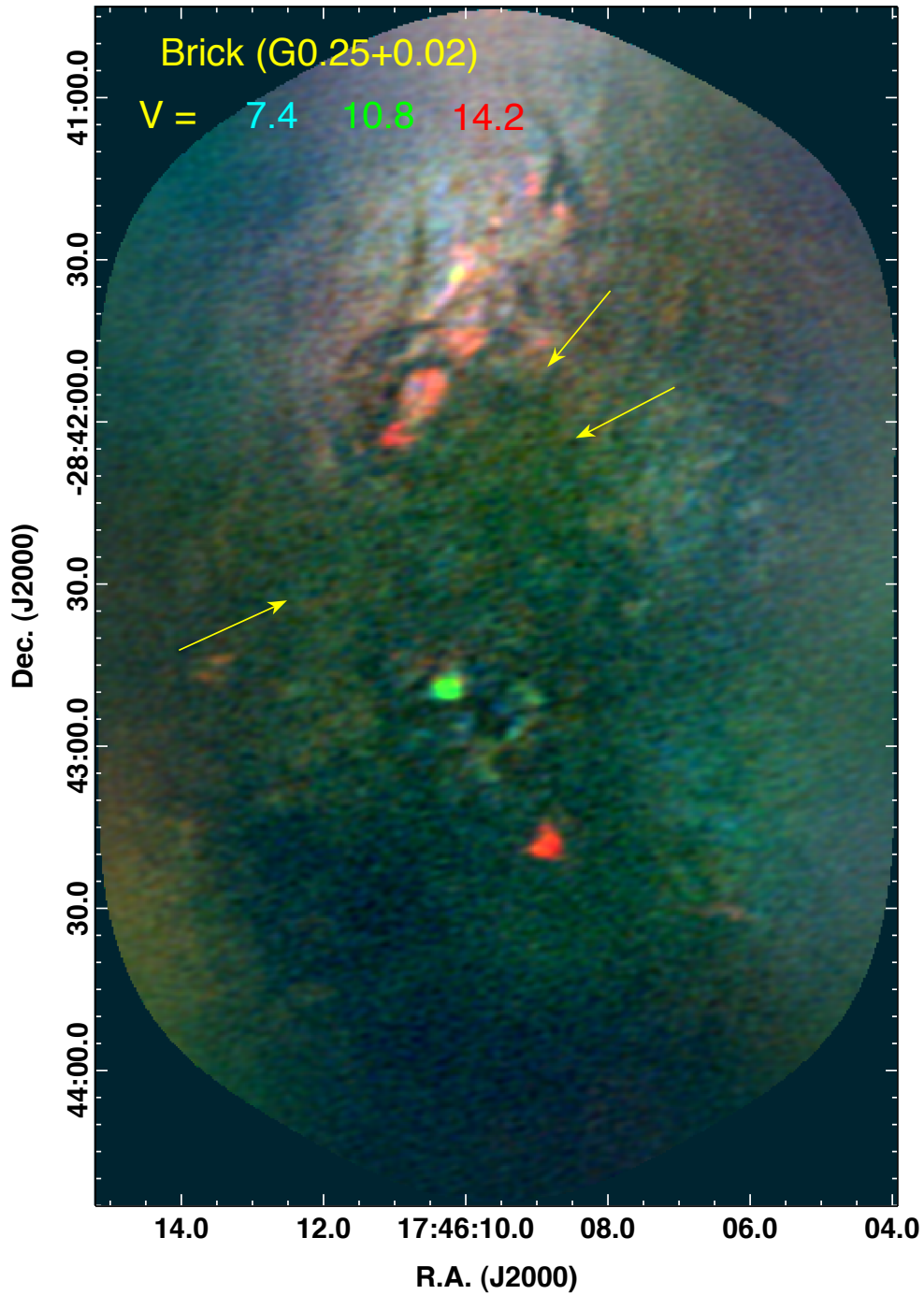
Fig. 2.— An HCO$^+$ image of G0.253+0.016 showing 3.4 km s^{-1} wide channels centered at V$_{\text{LSR}}$ = 7.4 (blue), 10.8 (green), and 14.2 (red) km s^{-1}. In addition to the arrows marking the location of the most BLA filaments, the three arrows in the lower-right mark the general locations of narrow line absorption (NLA) filaments in Figures 2 through 9.
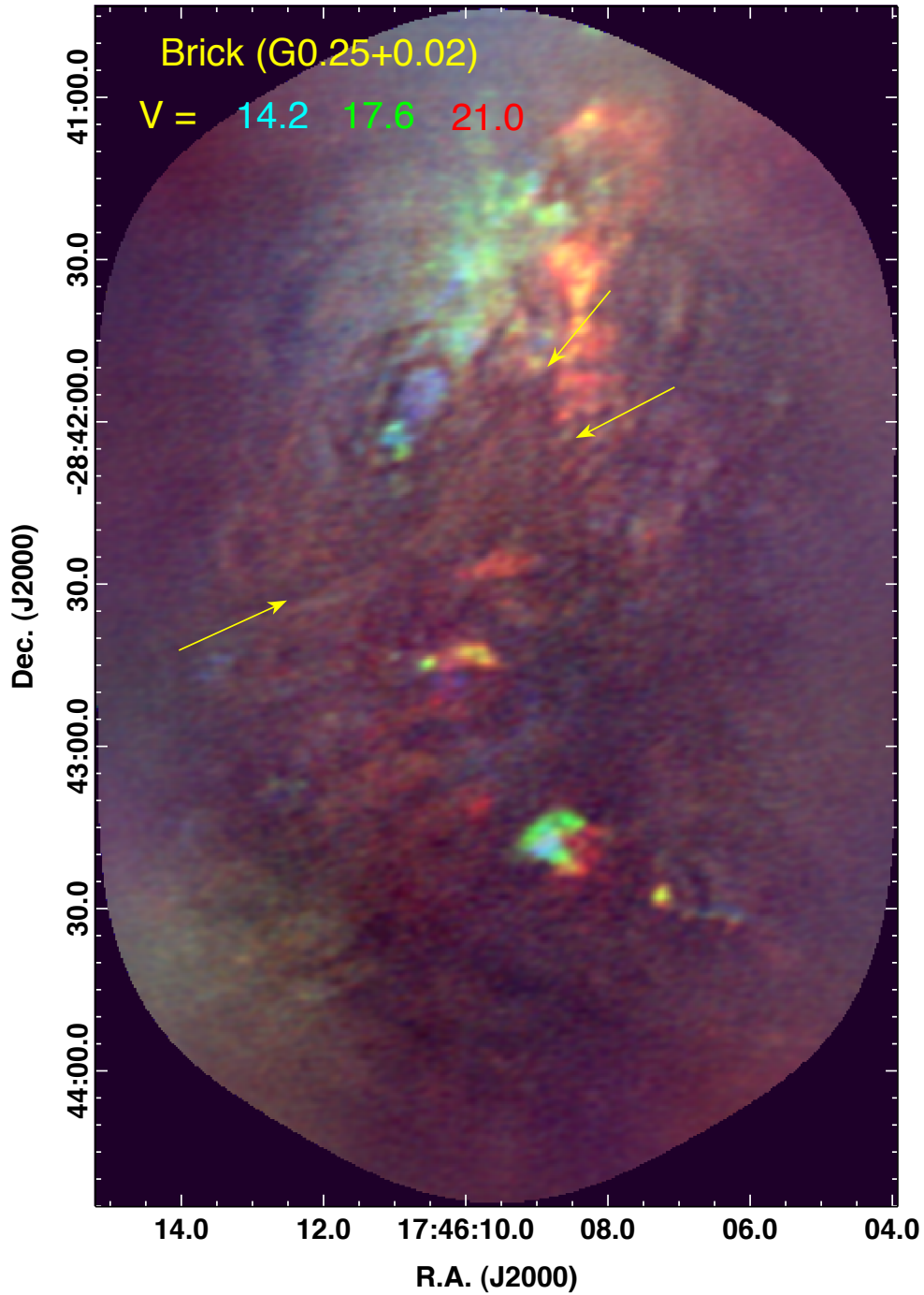
Fig. 3.— This figure shows HCO$^+$ channels centered at V$_{\mathrm{LSR}}$ = 14.2 (blue), 17.6 (green), and 21.0 (red) km s^{-1}.
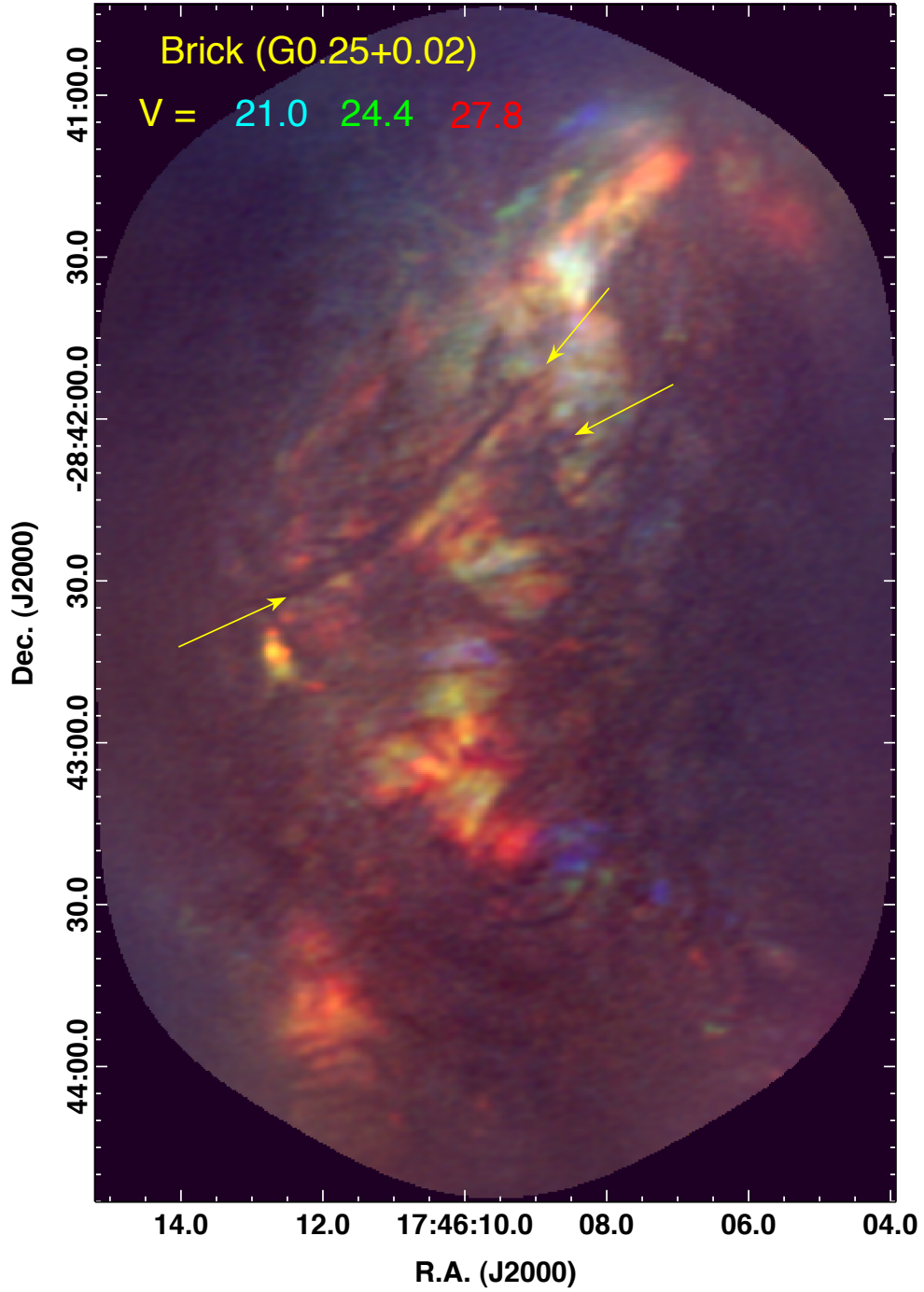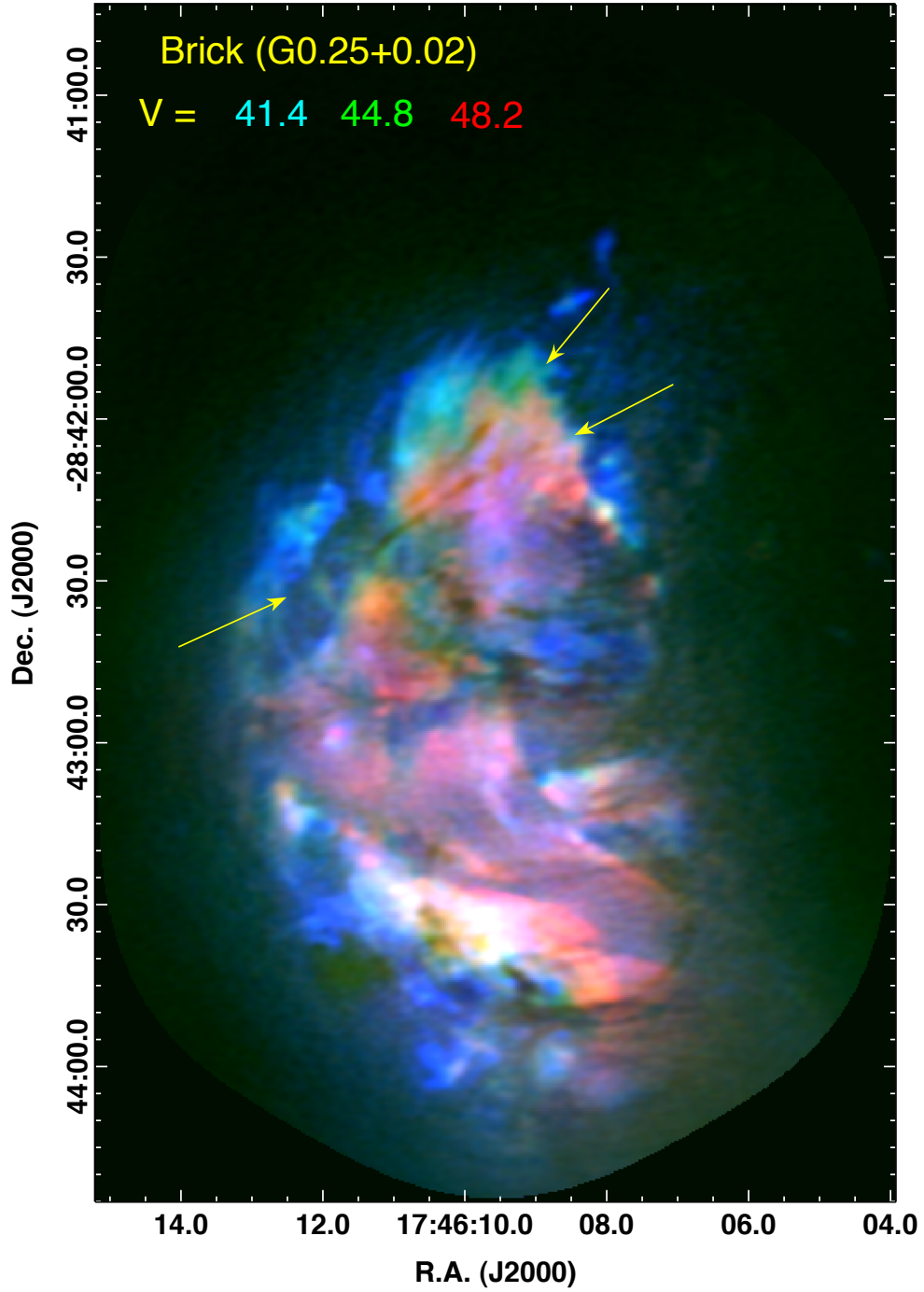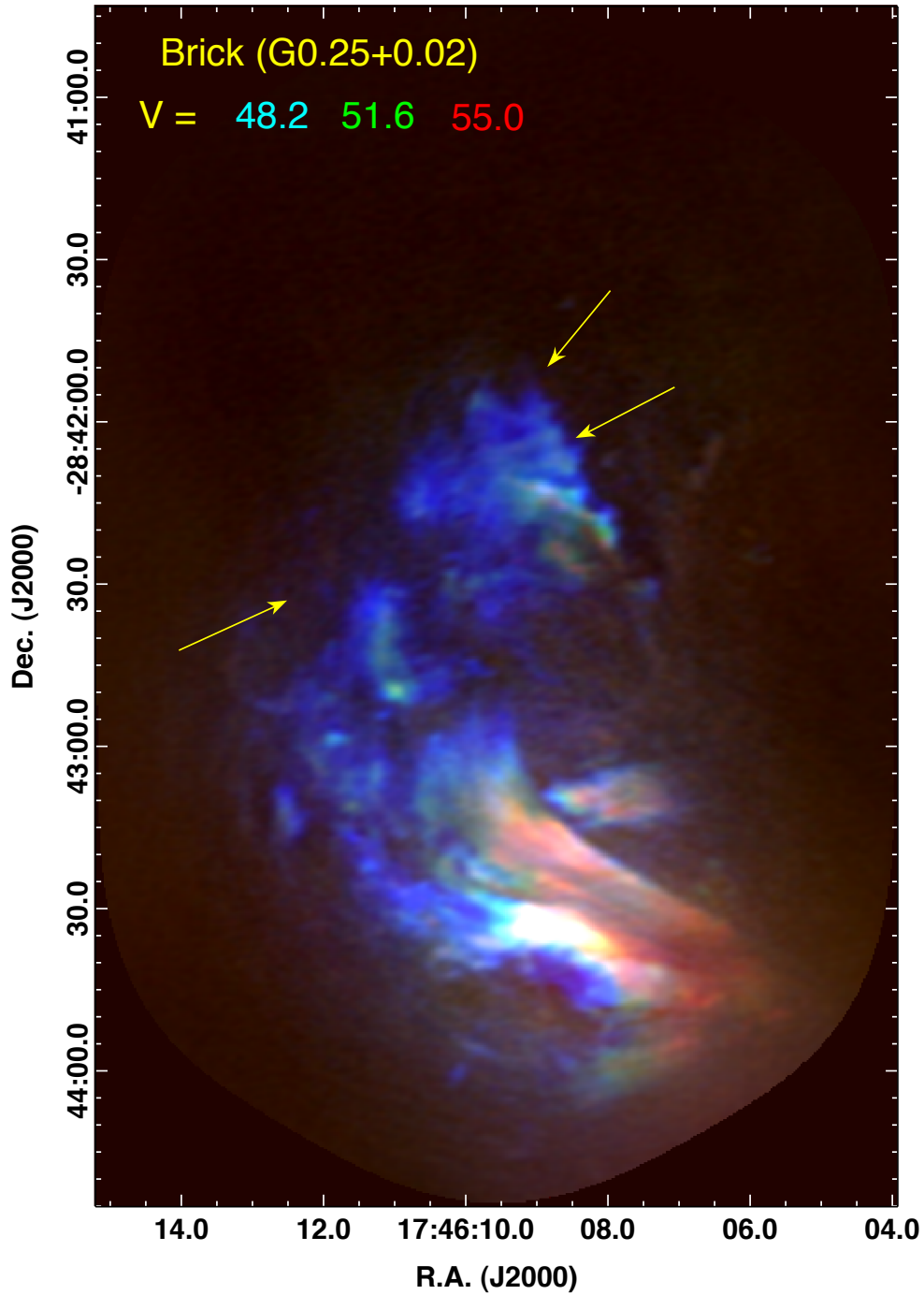
Fig. 4.— This figure shows HCO$^+$ channels centered at V$_{\mathrm{LSR}}$ = 21.0 (blue), 24.4 (green), and 27.8 (red) km s^{-1}.
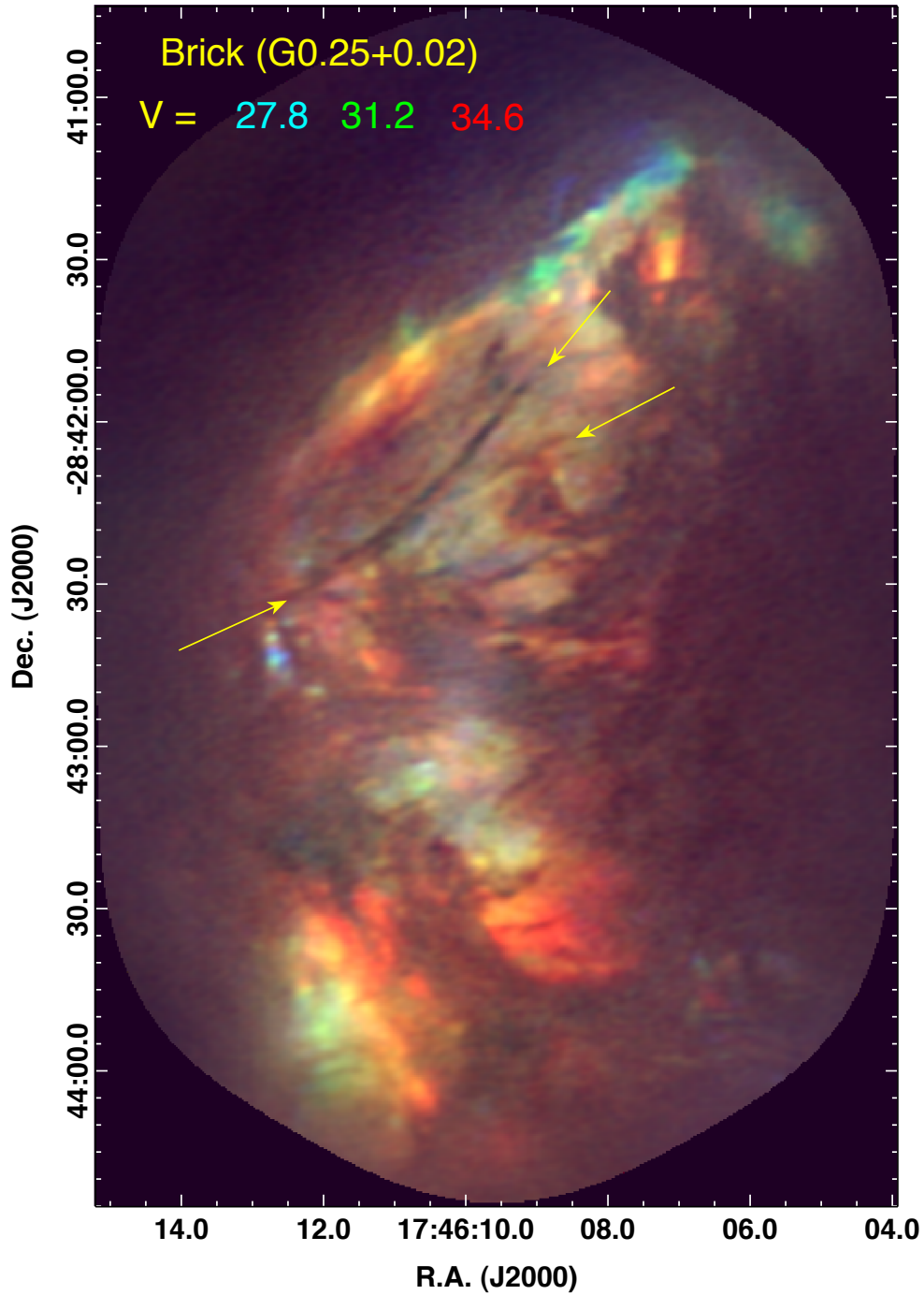
Fig. 5.— This figure shows HCO$^+$ channels centered at V$_{\mathrm{LSR}}$ = 27.8 (blue), 31.2 (green), and 34.6 (red) km s^{-1}.
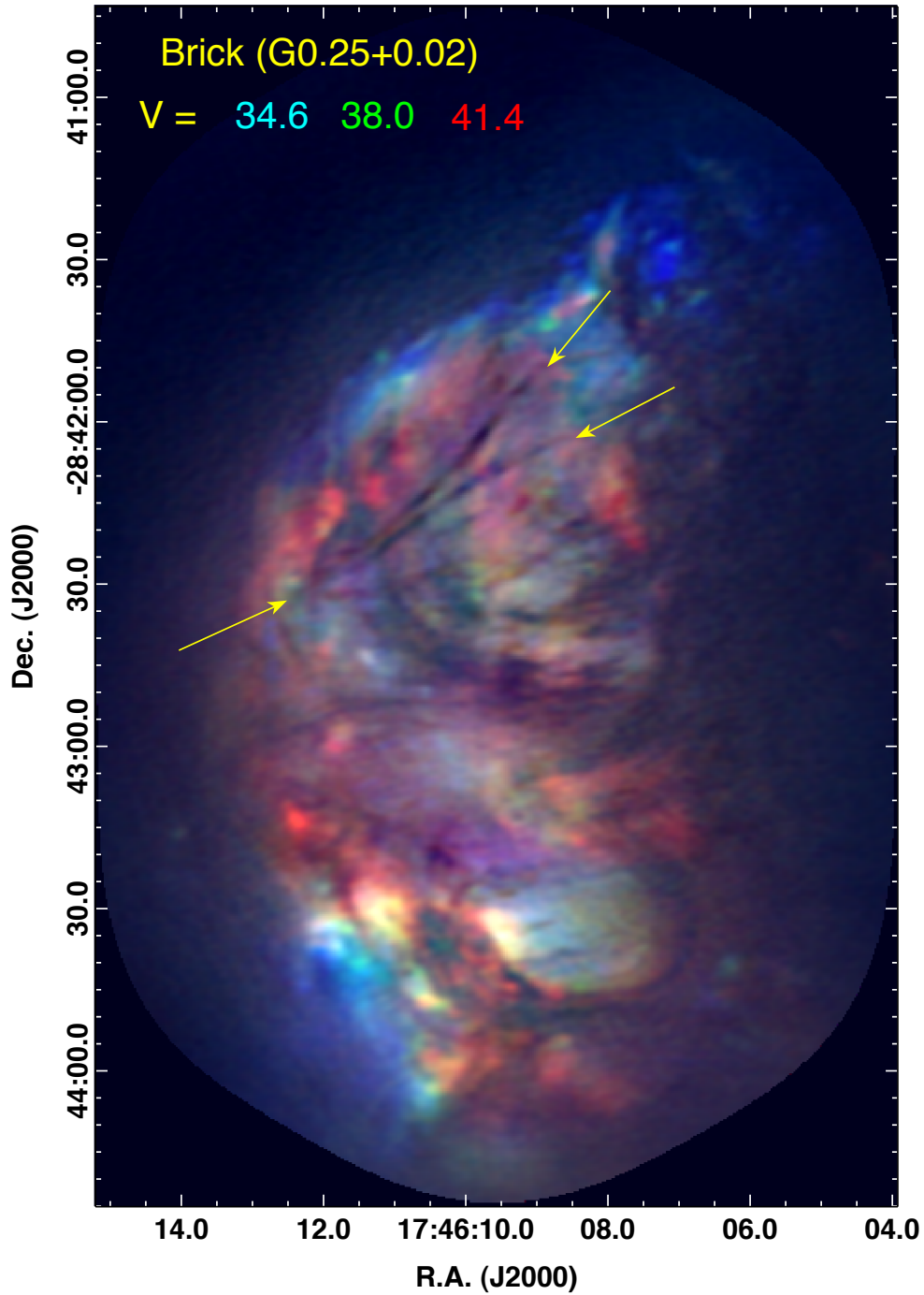
Fig. 6.— This figure shows HCO$^+$ channels centered at V$_{\mathrm{LSR}}$ = 34.6 (blue), 38.0 (green), and 41.4(red) km s^{-1}.

Fig. 7.— This figure shows HCO$^+$ channels centered at V$_{\mathrm{LSR}}$ = 41.4 (blue), 44.8 (green), and 48.2 (red) km s^{-1}.

Fig. 8.— This figure shows HCO$^+$ channels centered at V$_{\mathrm{LSR}}$ = 48.2 (blue), 51.6 (green), and 55.0 (red) km s^{-1}.
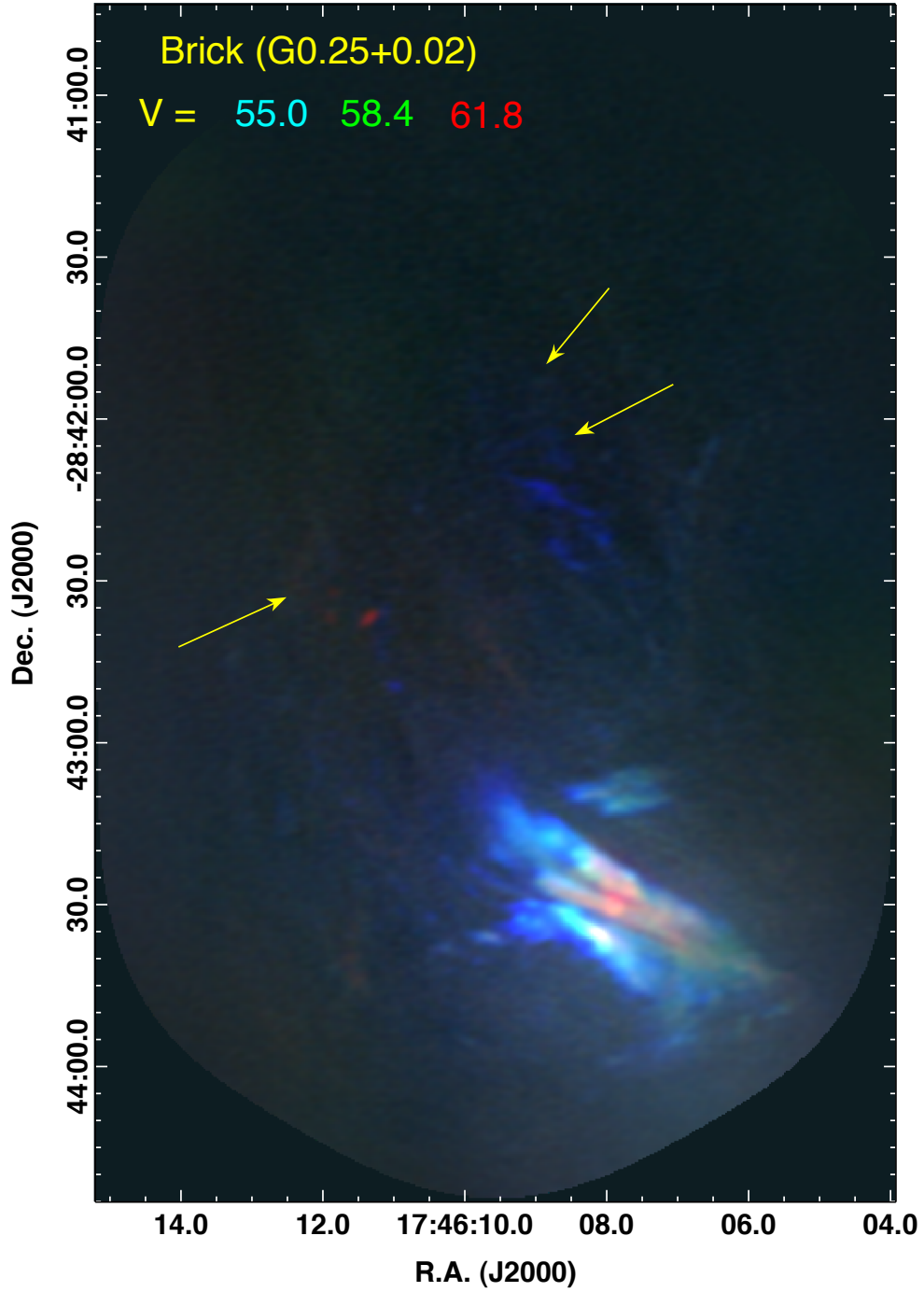
Fig. 9.— This figure shows HCO$^+$ channels centered at $V_{LSR} = 55.0$ (blue), 58.4 (green), and 61.8(red) km s^{-1}.
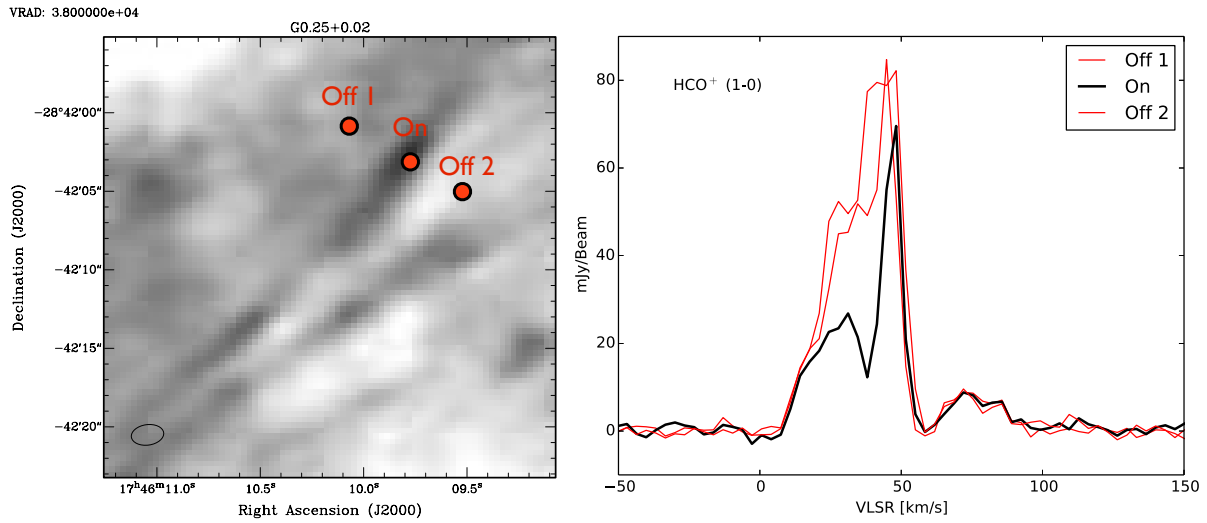
Fig. 10.— *(Left:)* The location of three HCO⁺ spectra shown in the Right panel *(Right:)* The HCO⁺ spectra shows the most prominent BLA absorption at the location labeled 'On' (thick black line) and two off positions (thin red lines).
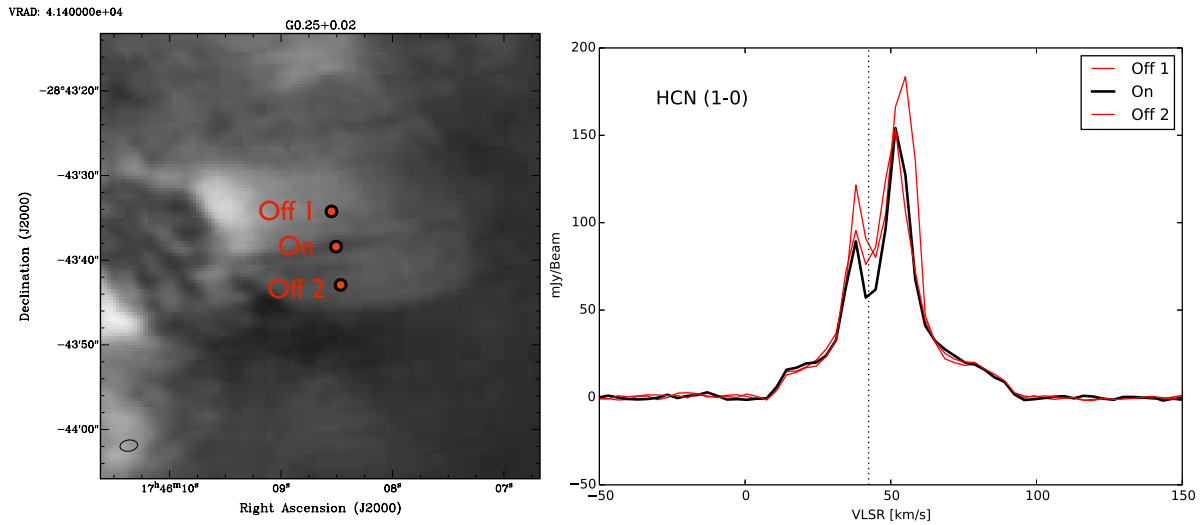

Fig. 11.— *(Left:)* The location of three HCN spectra shown in the Right panel *(Right:)* The HCN spectra shows an example NLA filament at the location labeled 'On' (thick black line) and two off positions (thin red lines). The dotted vertical line shows the central velocity of the absorption feature.
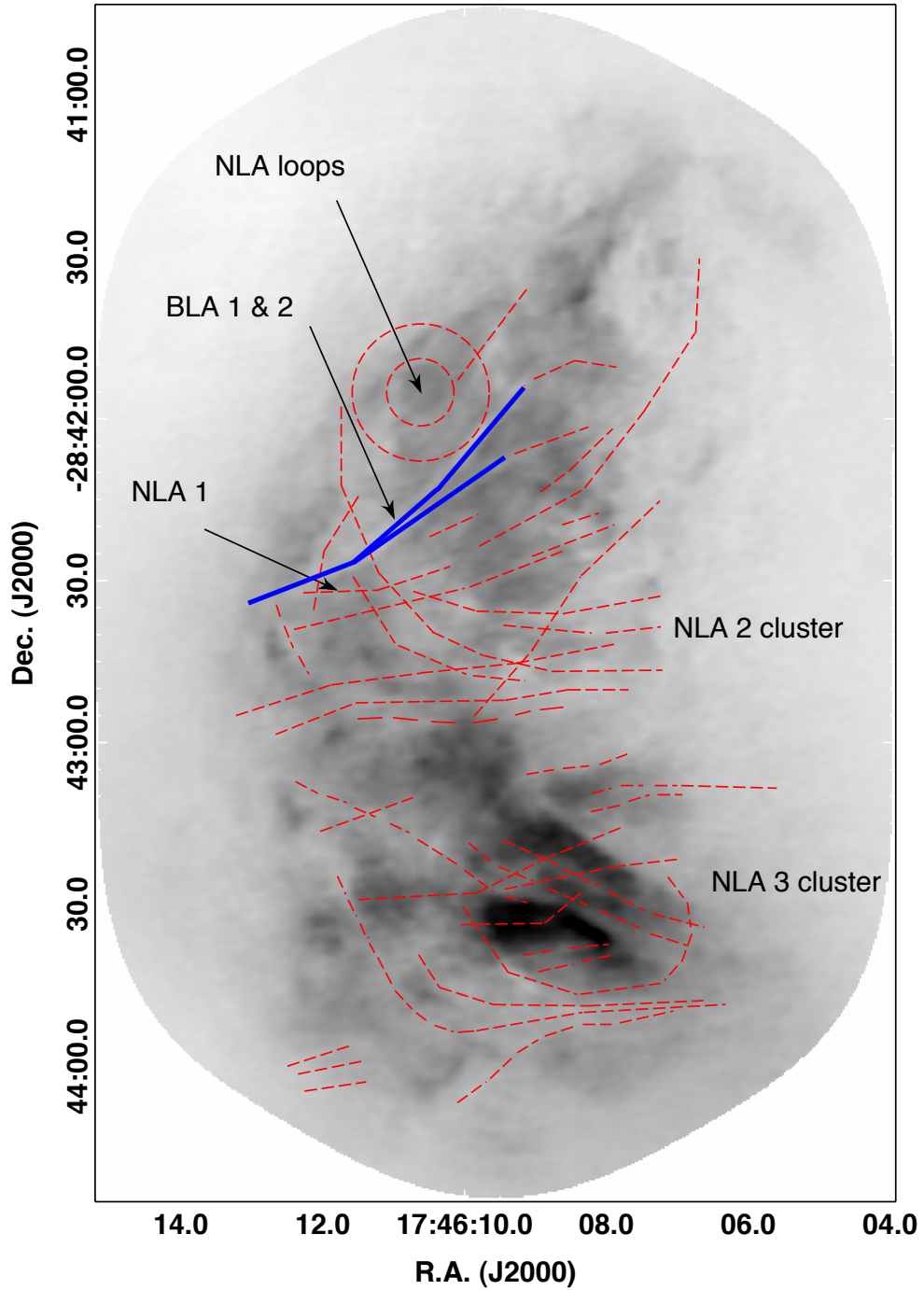
Fig. 12.— The image shown in Figure 1 with the locations of filaments superimposed. Thick solid lines show BLA filaments; thin dashed lines indicate locations of some of the NLA filaments.
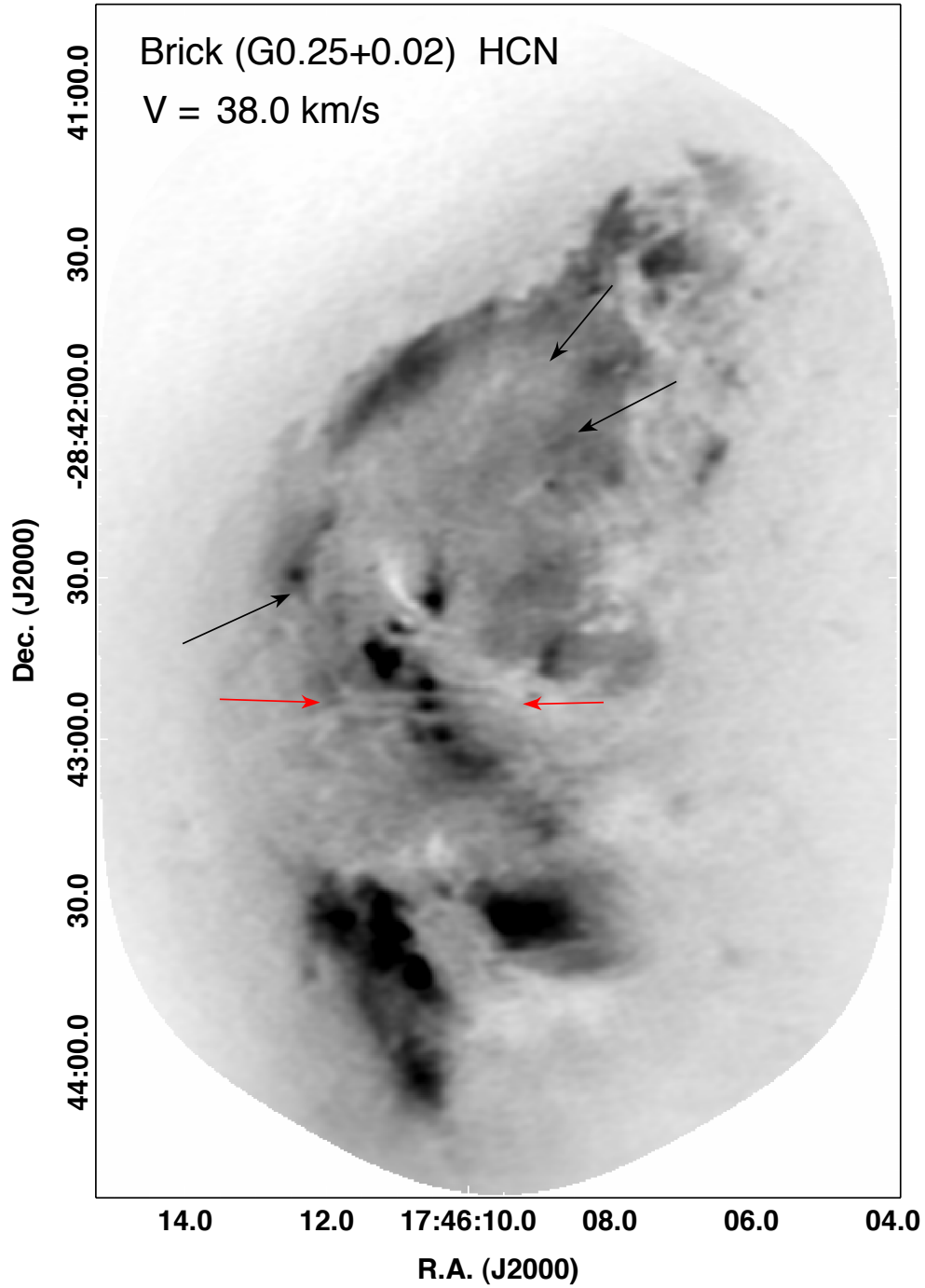
Fig. 13.— An HCN image at $V_{LSR} = 38.0$ km s^{-1} showing narrow-line absorption (NLA) filaments. The prominent broad line absorption (BLA) filaments seen in HCO$^+$ are not seen in this tracer. The two horizontal arrows mark the locations of several NLA filaments in the NLA2 cluster which also absorb in HCN.
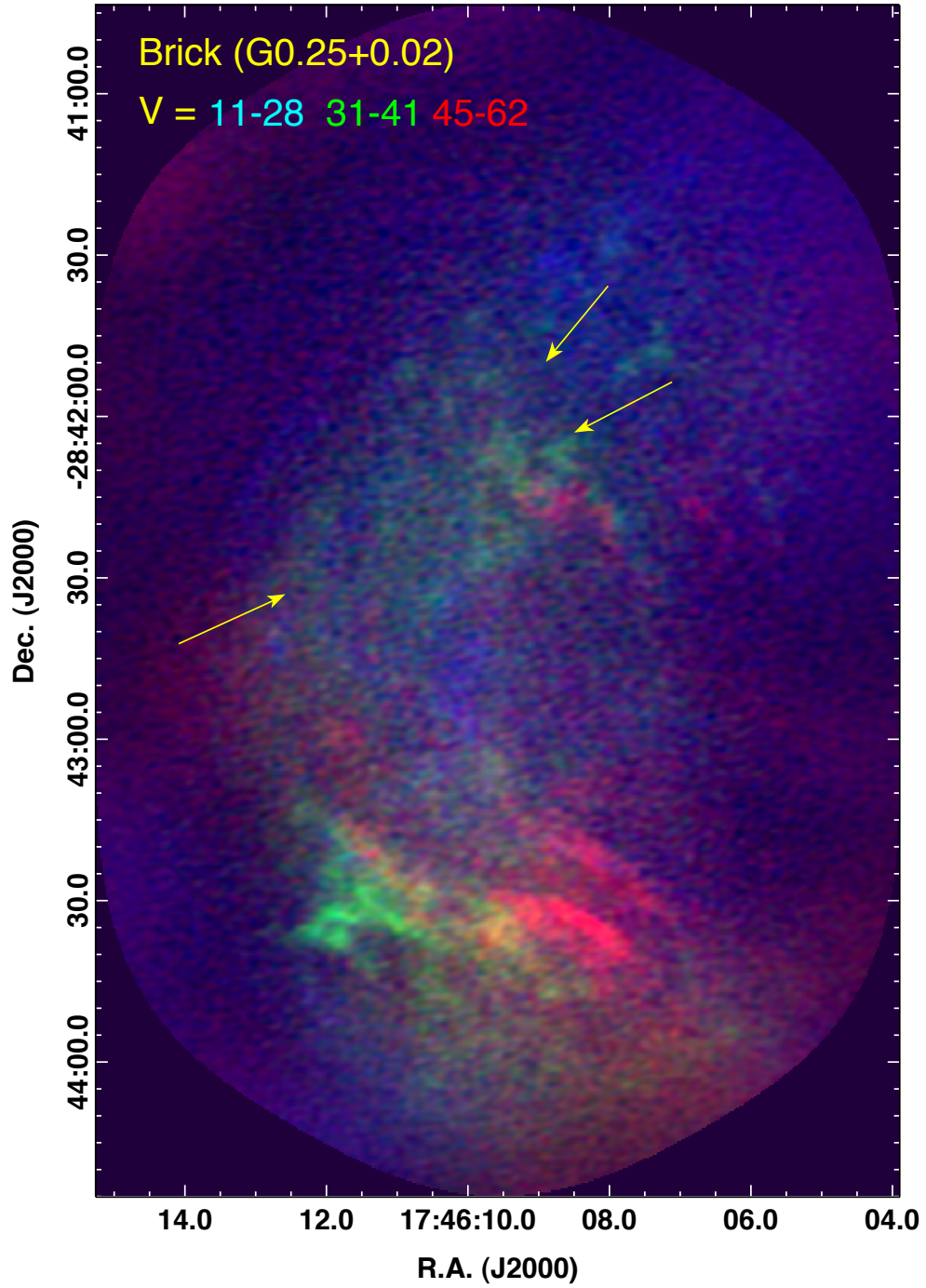
Fig. 14.— An H^{13}CO$^+$ RGB image showing the bow-shape of the Brick in an optically thin tracer. The velocity ranges (in km s^{-1}) for the blue, green, and red are indicated in the figure.
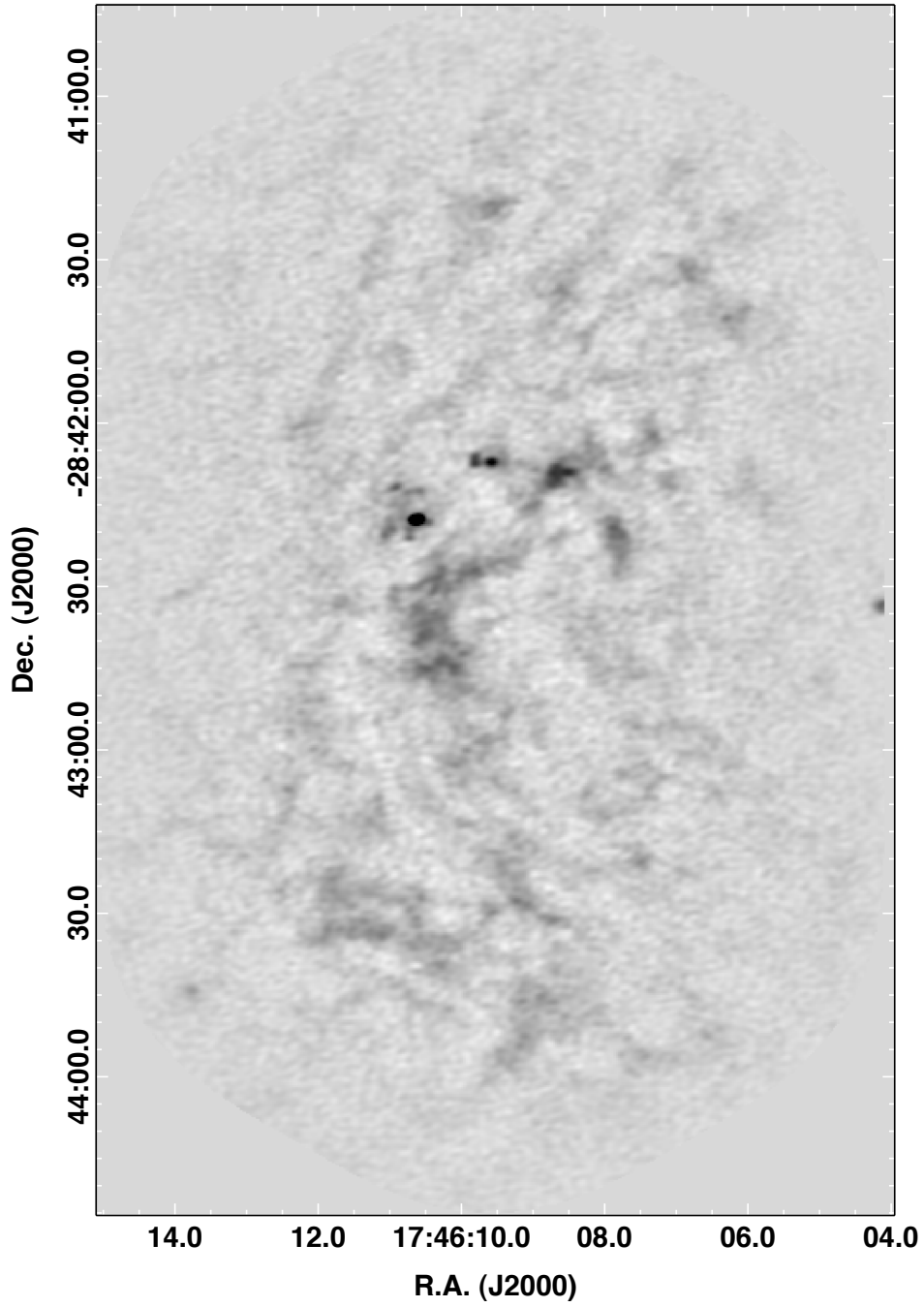
Fig. 15.— The 3 mm continuum emission from G0.253+0.016. The bright point upper left of center is associated with the H_2O maser source, located at J2000 = $17^h46^m10.62^s$, $-28°42'17.8''$. This image and its interpretation is discussed in detail in Rathborne et al. (2014a).

Table 1.   HCO$^+$ Selected Filaments in Absorption Towards the Brick.

α J2000	δ J2000	V$_{LSR}$ km s^{-1}	Comments
17:46:09.2	-28:41:54	21 to 45	BLA 1 Northwest end
17:46:10.6	-28:42:14	21 to 45	BLA1 core
17:46:11.8	-28:42:25	21 to 45	BLA 1 Southeast end
17:46:08.9	-28:42:05	21 to 45	BLA2 West end
17:46:09.9	-28:42:12	34 to 45	BLA2 core 1
17:46:11.1	-28:42:22	21 to 45	BLA2 core 2
17:46:12.9	-28:42:34	18 to 45	BLA2 East end
17:46:10.6	-28:41:55	11 to 21	6″ radius loop
17:46:10.6	-28:41:55	11 to 21	13″ radius loop
17:46:10.3	-28:42:28	31 to 38	NLA1 West end
17:46:11.9	-28:42:33	31 to 38	NLA1 East end
17:46:07.5	-28:42:50	21 to 45	NLA2 cluster; West end
17:46:11.7	-28:42:50	21 to 45	NLA2 cluster; East end
17:46:06.6	-28:43:46	31 to 48	NLA3 cluster; West end
17:46:10.6	-28:43:30	31 to 48	NLA3 cluster; East end

Table 2. RADEX[1] calculations for the J=1-0 HCO$^+$ transition.

$log\ n(H_2)$		T_{ex}			τ			T_R	
$log\ N(HCO^+)$	13	14	15	13	14	15	13	14	15
2.000	2.74	2.78	3.15	0.85	8.41	72.9	0.005	0.004	0.355
2.477	2.76	2.87	3.78	0.84	8.10	58.1	0.016	0.118	0.909
3.000	2.84	3.17	5.23	0.82	7.24	37.9	0.053	0.366	2.254
3.477	3.07	3.83	7.69	0.75	5.74	21.5	0.149	0.950	4.624
4.000	3.84	5.49	12.4	0.57	3.55	10.1	0.415	2.426	9.275
4.477	6.30	9.33	20.1	0.30	1.69	4.60	0.849	5.078	16.77
5.000	38.7	37.4	41.4	0.03	0.29	1.57	1.210	8.670	30.16
5.477	-19	-34	152	-0.04	-0.2	0.31	1.002	8.681	39.68

Note. — [1]: The tabulated values assume a background radiation temperature of 2.73 K, a gas kinetic temperature of 60 K, and a line-width of 10 km s^{-1}. Based on the on-line RADEX tool available at http://www.sron.rug.nl/∼vdtak/radex/radex.php.